Al-Hamdaniya Journal for Pure Sciences, Vol: 0, No: 0, 2025 (1- 8)

Backbending Of The 155 – 165Ho Isotopes Using A Modified Model

Malik. H. Kheder[1]*, Hanaa N. Azeez[2], Rajaa, A. Basheer[3]

[1*,2,3]Department of Physics, Education College for Pure Science, University of Al-Hamdaniya, Mosul, Iraq

E-mail: [1*] dr.malik73@uohamdaniya.edu.iq

Abstract

This research used a developed theoretical model that formulated to study the energy levels and the phenomenon of backbending of some nuclei $^{155-165}$Ho isotopes and compare them with the available practical results. The backbending of the moment of inertia for the ground state bands is successfully described and nuclear energy levels are calculated using a modified phenomenological model. When nuclei rotate, the Coriolis force operates to de-pair the nucleon pair and align their angular momentum with the nucleus's total angular momentum. This causes the Coriolis force to increase and decrease the rotational energy. The model accounts for the pairing effect with a constant moment of inertia. Thus, the angular momentum affects the moment of inertia. In order to make the moment of inertia change with angular momentum, a term was added to this model. When only a few parameters are used, the modified model frequently matches the experimental data quite well.

Keyword: Angular momentum, Backbending, Pairing effect, Moment of inertia, Ho isotopes.

1. Introduction

Backbending has been thoroughly investigated in numerous nuclei ever since it was shown to occur at high spins in the ground state rotational bands of even-even rare earth nuclei [1]. Numerous distorted nuclei have been reported to exhibit an abrupt drop in rotational frequency and an unusual increase in moment of inertia. Backbending is the phenomena where an S-shaped plot of twice the moment of inertia vs the square of rotational frequency for different spin states is observed [2]. In many light, medium, and heavy even-even nuclei, a number of models had achieved remarkable success in describing the low lying collective states. Over the past three decades, data for a significant number of high-spin nuclei has been gathered, and in some of these data, an intriguing effect has been seen in the ground state rotational band (yrast states) of some even-even nuclei [3]. One of these models, the variable moment of inertia (VMI) model, uses two parameters that Mariscottoi introduced to the rotational energy equation in order to fit the measured energies [4]. Several nuclei showed some notable departures from the VMI model in terms of the moment of inertia as well [5-9]. The other intriguing model is developed by Swiatecki and Myers [10]. The energy of initially counter-rotating gyroscopes that cause the overall rotation to gradually align in the direction of the total angular momentum, a potential energy that prevents such alignment, and a rigid rotation of a portion of the nucleus make up the basis of this model. The model contains differences from experimental energies but can be used to describe the angular momentum dependence of nuclear rotational energy at a macroscopic level. The models, angular momentum projected Tomm–Dancoff approximation, and backbending were used in the most current computations [11]. Interaction between neutrons and protons under the Bardeen–Cooper–Schrieffer (BCS) model [12]. model of the predicted shell [13]. and the projected configuration interaction (PCI) approach, which directly links shell model wave functions to the deformed intrinsic states [14].

2. Research Method

In our developed model, we relied on the Cranked Shell model (CSM) and the Variable moment of inertia (VMI) model, as in the Cranked model the Hamiltonian of the plane is given by equation [15].

$$H^{-} = H - \blacksquare\,\omega J_{X} \tag{1}$$

As H is the Hamiltonian of the plane and $-\blacksquare\,\omega J_{X}$ represents the Coriolis force that works to align the angular momentum of the nucleons towards the angular momentum of the rotating nucleus, which also works to break the pairing of the nucleons, and considering that H is the Hamiltonian according to the Nilsson model, which is given by the following equation:

$$H = H_{o} + C\sum_{i} L_{i}\cdot S_{i} + D\sum_{i} L_{i}^{2} \tag{2}$$

It is the Hamiltonian spin, and the second term $(l\cdot s)$ is the spin-orbit interaction for the single nucleon. The third term represents the interplaing between the square well voltage and the harmonic oscillator voltage, and C, D are experimental constants [16], and thus the result becomes :

$$H^{-} = H_{o} - \blacksquare\,\omega J^{X} + C\sum_{i} L^{i}\cdot S^{i} + D\sum_{i} L_{i}^{2} \tag{3}$$

Since: $H\psi = E\psi$ It produces [17]:

$$E = E_0 - \blacksquare\,\omega J_X + C\sum_i L_i \cdot S_i + D\sum_i L_i^2 \qquad (4)$$

Considering that E_0 is the sum of the rotational energy of the variable moment of inertia model E(J)VMI, the pair energy E Pair, and the energy of the single particle ES.P that is:

$$E_0 = E(J)_{VMI} + E_{Pair} + E_{S\cdot P} \qquad (5)$$

By adding the couple energy, the single particle energy, and the rotational energy to the variable moment of inertia model, the total energy equation becomes:

$$E(J) = E(J)_{VMI} + E_{Pair} + E_{S.P} - \blacksquare\,\omega J_X + C\sum_i L_i \cdot S_i + D\sum_i L^2{}_i \qquad (6)$$

The last term takes the following value: since

$$J = L \mp S$$

$$L^2 = l(l+1) \Rightarrow L^2 = (J+S)(J+S+1) \Rightarrow (J+1/2)(J+3/2)$$

$$\therefore D(L^2) = D(J+1/2)(J+3/2)$$

$$L\cdot S = \frac{1}{2}(J^2 - L^2 - S^2) \Rightarrow L\cdot S = \begin{cases} \frac{1}{2}L & if \quad J = L+S \\ \frac{-1}{2}(L+1) & if \quad J = L-S \end{cases}$$

$$C\sum_i L_i \cdot S_i = C\left(\frac{-1}{2}(L+1)\right) = C\left(\frac{-1}{2}(J+3/2)\right) \qquad (7)$$

As for the term representing the Coriolis force, it is the component of angular momentum in a direction perpendicular to the rotation axis and is equal to:

$$\blacksquare\,\omega J_X = 41A^{-1/3}\sqrt{J(J+1) - K^2} \qquad (8)$$

This equation gives good results for low excitation levels up to a certain angular momentum, which is the segmental momentum J_C, at which a pair of neutrons, as a result of the increasing Coriolis force, become uncoupled and begin to align with the momentum of the nucleus [18].

The momentum of the cut is equal to:

$$J_C = \frac{N-Z}{2} + T \qquad (9)$$

Then, N is the number of neutrons in the nucleus, Z is the number of protons in the nucleus, and T is the correction factor between the theoretical and practical values or the matching constant between them. When the excitation levels are less than the break-off momentum, the proton pairing energy is greater than the neutron pairing energy. Therefore, at this momentum, the coupling is broken. A pair of neutrons, which leads to the appearance of back bending. However, at high excitation levels, that is, after the momentum of the break, the energy of the single particle becomes Because the nucleus had one single particle, and after disengaging a pair of neutrons, two particles were added to the single particle, so it became three single particles (3-qp), and the pairing energy after disengaging a pair of neutrons becomes Because the binding energy of the next pair of neutrons becomes twice the energy of the first pair, which is more than the pairing energy of a pair of protons. Therefore, with increasing excitation, the probability of disengaging a pair of protons increases, and this leads to the appearance of a second back bend.

So, in the presence of a cut-off frequency, the energy equation will have two parts before and after the cut-off frequency [19]:

$$E(J) = \frac{J(J+1)}{2I(J)} + F\{-\frac{1}{2}(I(J) - I_0)^2 + \varepsilon_0 (J-K) + E_{n.Pair} - \hbar\omega_X J + C_1(\frac{-1}{2}(J+\frac{3}{2})) + D_1(J+\frac{1}{2})(J+\frac{3}{2})\} \qquad IF\ J \le J_C$$

$$E(J) = \frac{J(J+1)}{2I(J)} + F\{-\frac{1}{2}(I(J) - I_0)^2 + 3\varepsilon_0 + 2E_{n.Pair} + E_{P.Pair} - \hbar\omega_X J + C_2(\frac{-1}{2}(J+\frac{3}{2})) + D_2(J+\frac{1}{2})(J+\frac{3}{2})\} \qquad IF\ J > J_C \tag{10}$$

Through the difference between two successive levels, we obtain the value of the gamma energy, and by calculating it, we can calculate the variable moment of inertia from equation [20].

$$\frac{2I}{\hbar^2} = \frac{4J-2}{E(J)-E(J-2)} \tag{11}$$

then calculate the rotational frequency, which is given by equation [21].

$$\hbar w = \frac{E(J)-E(J-2)}{\sqrt{J(J+1)} - \sqrt{(J-2)(J-1)}} \tag{12}$$

by drawing the relationship Graphing the values of the variable inertia moment on the y-axis and the values of the rotational frequency on the x-axis, we get the backbend.

3. Results And Discussion

The parameter and constant values used for each isotope included in Table 1. And Figure 1. This nuclei has 67 protons, including 3 protons in the 2d3/2 shell, which can accommodate 4 particles. Therefore, it also occupies more than half of the shell, so n2=1 is equal to the number of gaps in the shell, and the value of s1=2, s2=1, and T=3, and these values It is the same for all isotopes of this nucleus.

Table 1. The parameter and constant values used for each isotope

isotope	β	f	C1	D1	C2	D2
Ho-155	0.200	0.00645	40.5	1.15	18.3	0.6
Ho-157	0.217	0.006369	20.65	0.6	1.6	0.41
Ho-159	0.242	0.006289	41.9	0.85	25.3	0.74
Ho-161	0.25	0.006211	22.4	0.42	7.8	0.52
Ho-163	0.258	0.006134	43.25	1	—	—
Ho-165	0.267	0.006061	21.9	0.37	—	—

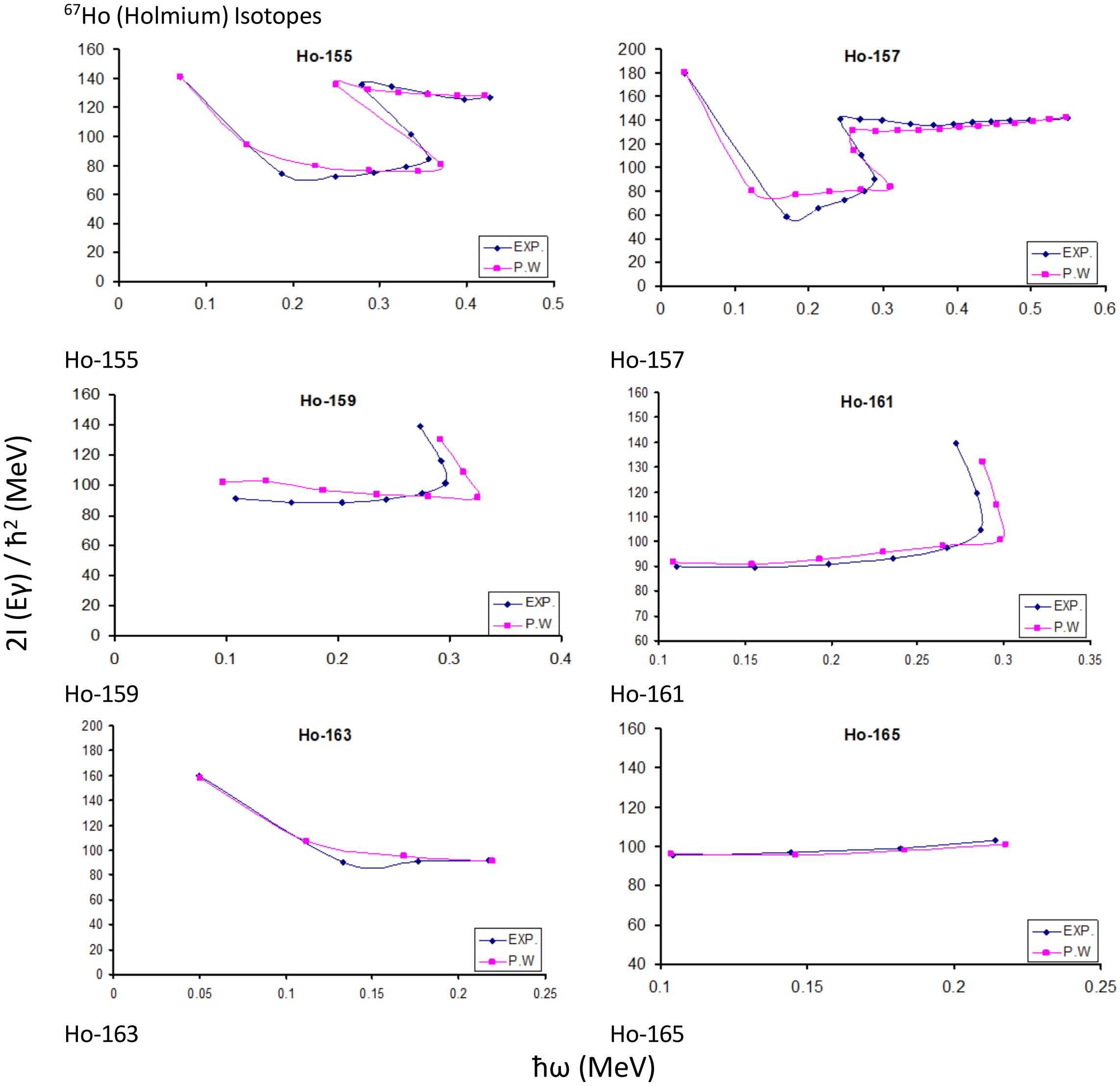

Figure 1. Holmium isotopes backbending.

The isotope (155Ho) has 88 neutrons, including 6 neutrons in the outer shell 1h9/2, which accommodates ten particles, meaning that the six neutrons for this isotope occupy more than half of the shell, so n1=4 is equal to the number of gaps in the shell, and the value of the beginning of the beam $\pi h_{11/2}$ for this isotope is equal to k=11/2 and the value of the torque $I_0 = 67.05148$, the inertia at zero angular momentum is equal to 1h9/2, and the cutting momentum that disengages a pair of neutrons in the shell is practically equal to 1h9/2. =10.5 Theoretically J_c= 27/2=13.5, this means that the constant of matching between theoretical values and practical values is equal to T=3. The change between the moment of inertia with the rotational frequency I □ 136.0117. We notice from it that the practical and theoretical curves start with a large value and then decrease because the gamma energy is low in the beginning, which leads to a large value for the moment of inertia. After reaching the middle of the curve, the moment of inertia begins to increase again until it reaches to rotational frequency □□ □ 0.24987. Then the rotational energy suddenly decreases as a result of the disengagement of a pair of neutrons and the alignment of their angular momentum with the angular momentum of the nucleus, which leads to a decrease in gamma energy and an increase in the moment of inertia. Therefore, back bending occurs and the value of the moment of inertia is, and then the rotational frequency begins to increase again and in harmony, good agreement with practical values. The isotope (157Ho) has 90 neutrons, including 8 neutrons in the outer shell 1h9/2, which accommodates ten particles, meaning that the eight neutrons for this isotope occupy more than half of the shell, so n1=2 is equal to the number of gaps in the shell, and the value of the beginning of the beam for this isotope is equal to, and the value of the torque The inertia at zero angular momentum is equal to 1h9/2, and the cutting momentum that disengages a pair of neutrons in the shell is practically equal to 1h9/2. The isotope (159Ho) has 92 neutrons, including 10 neutrons in the outer shell 1h9/2, which accommodates ten particles, meaning that the ten neutrons for this isotope occupy the entire shell, so n1=0 is equal to the number of gaps in the shell that does not have a gap. The value of the beginning of the beam for this isotope is equal, the value of the moment of inertia at zero angular momentum is equal, and the momentum of the break that disengages a pair of neutrons in the shell is practically equal to 1h9/2. The isotope (161Ho) has 94 neutrons, including two neutrons in the outer shell 2f7/2, which accommodates eight particles, meaning that the two neutrons for this isotope occupy the beginning of the shell, so n1=2 is equal to the number of particles in the shell, and the value of the beginning of the beam for this isotope is equal to, and the value of the moment of inertia at momentum. The isotope (163Ho) has 96 neutrons, including 4 neutrons in the outer shell 2f7/2, which accommodates eight particles, meaning that the four neutrons for this isotope occupy half the shell, so n1=4 is equal to the number of particles in the shell, and the value of the beginning of the beam for this isotope is equal to, and the value of the moment of inertia. The isotope (165Ho) has 98 neutrons, including 6 neutrons in the outer shell 2f7/2, which accommodates eight particles, meaning that the six neutrons for this isotope occupy more than half of the shell, so n1=2 is equal to the number of gaps in the shell.

4. Conclusion

We notice from the figure that there is great agreement between the results obtained from this model with the practical results obtained from the Atomic Energy Organization taken from the reference [22].

This means that the developed model has the ability to calculate the level energies and back curvature of individual nuclei of mass number with high accuracy using some appropriate fitting constants.

Since the model succeeded in calculating the back curvature of odd-numbered nuclei, which is difficult to calculate, it is certain that the model can calculate the back curvature of even-even nuclei

5. Acknowledgements

The authors would like to thank the University of Al-Hamdaniya / College of Education for Pure Sciences, which have helped to enhance the quality of this work.

6. References

[1] Johnson . A , Ryde . H , Sztarkier . J , (1971) , " Evidence for a singularity in the nuclear rotational band structure " Phys. Lett. B , 34(7) : 605-608.

[2] Sun Y. and Hara K. , (1998) , " Theoretical reinvestigation of high spin spectroscopy of 164Er ", Phys. Rev. C , vol.57 , no.6 , pp.57.

[3] Alhendi . H , Alharbi . H , EL-Kameesy . S , (2008) " Improved exponential model with pairing attenuation and the backbending phenomenon " , arxiv: Nucl-th/0409065v4.

[4] Mariscotti . M , Gertrude Scharff-Goldhaber , Brain Buck , (1969) , " Phenomenological analysis of ground state bands in even-even nuclei ", Phys. Rev. , 178(4):1864-1887.

[5] Lin . L , (1978) , "The high-spin anomaly in rotational nuclear states ", Chinese . J . Phys. Vol.16 , no. 2,3 , pp.157.

[6] Al-Malki M. H., (2005) Nuclear Structure Properties of Some Deformed Nuclei in the Region of Mass Number A ≈ 150, M. Sc. Thesis (University of King Saud, Riyadh, Kingdom of Saudi Arabia, 2005).

[7] Riley . M , Aguilar .A , Evans .A , Hartley . D , Lagergren . K ,Ollier .J , Paul . E , Pipidis . A , Simpson . J , Teal . C , (2009) , "Strongngly deformation nuclear shapes at ultra-high spin and shape coexistence in N~90 nuclei " ACTA Physica Polonica B , Vol.40.

[8] Bengtsson . R & Frauendorf . S , (1979) , " An interpretation of Backbending in terms of crossing of ground state band with an Aligend two quasi particles band " , Nucl. Phys. A ,314 : 27-36.

[9] Amita Dua , Arun Bharti , Khosa . S , (2007) , " A microscopic study of deformation systematics in isotopes " Pramana . J . Phys. Vol. 68 , no. 6 , pp.1013.

[10] Myers . W & Swiatecki . W , (1998) , " Amicroscopic model of nuclear rotation ", ACTA Physica Polonica B , vol.29 , no.1-2 , pp.313.

[11] Sun . Y , (2004) , " Projected shell model study on nuclei near the N=Z line " Eur. Phys. J . A , vol.20 , pp.133-138.

[12] Ching-Tasi L . , Yang Sun , Jing-ya Zhang , Mike Guidry , Cheng-Li Wu , (2002) , " Microscopic description of band structure at very extended shapes in the mass region ", Phys. Rev. C , vol.65 ,pp.41301.

[13] Moller . P , Bauer . R , Becker . J , Bernstein . L , Carpenter . M , Durell . J, (1995) , " Calculated Nuclear Ground-State Masses and Deformations " , Atomic and Nuclear Data Tables , vol.59, no.2.

[14] Biniam Z . T . , (2006) " Super deformed Nuclei Bands and Exotic Nuclear Shapes ", Thesis of Ph.D , African Institute for Mathematical Sciences , Cape Town , South Africa.

[15] Bohr AAGE , (1975) , " Rotational motion in nuclei " Nobel lecture , the Niels Bohr institute and Nordita , Copenhagen . Denmark.

[16] Andgren K. , (2006) , " Lifetime measurements of Excited states in 165Lu and 107Cd", Licentiate Thesis in Physics , Stockholm , Sweden.

[17] Yamamoto . A . D , (2004) , " High spin structure of transitional nuclei around mass 100 " , A thesis of Doctor of Philosophy , Surrey University.

[18] Sukhjeet Singh , Malik . S , Kumar Jain . A , Singh . B , (2005) , " Table of three-quasiparticles rotational bands in deformed nuclei " Guru Nanak Dev Univ. Amritsar , India.

[19] Dean . D. J , Hjorth-Jensen .M , (2003)," Pairing in nuclear systems : from neutron stars to finite nuclei",Rev.of.Mod. Phys. , vol.75 , pp.607.

[20] Wong .S.S.M , (1990) , " Introductory Nuclear physics " , Prentice-Hall International , Inc. , U.S.A.

[21] Sorensen . R . A , (1973) , " Nuclear Moment of Inertia at high spin ", Rev. Mod. Phys. Vol.45 , no.3 , pp.353-376.

[22] Fireston . R . B , (1999) , " Table of Isotopes " 8th Edition , John Wiley & Sons , U.S.A.

Al-Hamdaniya Journal for Pure Sciences, Vol: 0, No: 0, 2025 (1-8)

Mixed Spin Ising Model in Binary System Under the Effect of an External Magnetic Field

Malak Jaafar Ali[1], Siham J. AL-Faris[2] Hasan F. Alturki[3]

[1,2]Department pf Physics, college of education for pure science, Al-Hamdaniya university

[3]Department of Medical Physics and Radiotherapy Engineering, College of Engineering Technology, Sawa University, Al Muthanna, Iraq.

E-mail: [1]malak.jaafar.ali@uohamdaniya.edu.iq, [2]siham.jasim@uohamdaniya.edu.iq,

[3]Hssnmugetsu@gmail.com

Abstract

In this study, we investigate the magnetic properties and compensation behaviors of a mixed spin-(3/2,7/2) Ising ferrimagnetic system on a square lattice using the mean-field approximation. The effects of crystal field anisotropy on the thermal variation of sublattice and total magnetization are analyzed. Our findings reveal the presence of various compensation types, including L, M, N, P, Q, R, and S, depending on the exchange interactions and crystal field parameters. These distinct compensation behaviors arise from the interplay between sublattice magnetizations, leading to unique temperature-dependent magnetic phase transitions. The results provide valuable insights into the thermodynamic stability of mixed-spin systems and their potential applications in spintronic devices and magnetic memory storage.

Keywords: Ising model, Mixed spin, Ferrimagnetism, Mean-field theory, Compensation behavior, Crystal field anisotropy.

1-Introduction:

Ferrimagnetic materials have many useful technological applications in information storage devices [1] and many other applications [2-5], the magnetic properties of mixed spin Ising ferrimagnets have been investigated different systems, such as [6-9]. Magnetic materials with mixed-spin configurations have gained significant attention due to their diverse physical properties and potential applications in spintronics, data storage, and magnetic sensors. Among these materials, ferrimagnetic systems composed of different spin values exhibit unique thermal and magnetic behaviors, including compensation phenomena and complex magnetization transitions. These behaviors are crucial in designing temperature-controlled magnetic devices, making them an essential area of theoretical and experimental research. The Ising model, particularly in the context of mixed-spin systems, provides a powerful framework for studying such magnetic behaviors. Using the mean-field approximation (MFA), researchers have successfully analyzed various thermodynamic properties, such as magnetization, phase transitions, and hysteresis effects, in low-dimensional and nanostructured materials. A high mixed spin-7/2 and spin-3 study was performed by H. Bouda et al. with periodic boundary conditions via Monte Carlo simulations. Establishing the phase diagram and generating compensation points while showing several topologies of the total magnetization [10]. Another high spin-7/2 and spin-1/2 system was performed by A. El Antari et al. used the framework of both the renormalization group technique and Monte Carlo simulation to examine the influence of an external magnetic field on the magnetic properties and hysteresis loop of the system [11]. The hysteresis and compensation behaviors of spin-3/2 cylindrical Ising nanotubes have been studied via effective field theory with correlations, and they reported that multiple hysteresis behaviors are strongly influenced by core–shell coupling, shell surface interactions and crystal fields [12]. One of the most intriguing aspects of these systems is the compensation effect, where the total magnetization vanishes at a temperature lower than the critical temperature T_C. This effect is highly sensitive to crystal field anisotropy, exchange interactions, and external perturbations. Several types of compensation behaviors have been classified in ferrimagnetic systems, including L, M, N, P, Q, R, and S types, each representing different temperature-dependent magnetization trends. Understanding these behaviors is fundamental for optimizing thermal stability and magnetic switching in advanced materials. Previous studies have extensively investigated mixed-spin systems with various spin combinations, such as (1/2, 1), (1, 3/2), and (1, 2), but less attention has been given to higher spin values like (3/2, 7/2), which can exhibit richer magnetic dynamics. In this work, we explore the magnetic properties and compensation behaviors of a mixed spin-(3/2, 7/2) Ising ferrimagnetic system on a square lattice using mean-field theory. We analyze the impact of crystal field anisotropy on the thermal variation of magnetization and identify different compensation types. Our results provide insights into the interplay between magnetic interactions and temperature-dependent phase transitions, offering valuable perspectives for future applications in magnetic memory storage and spintronic devices.

2- Model:

We consider two-dimensional Ising model with spins, Si = ±7/2, ± 5/2, ± 3/2, and ± 1/2 and Sj = ±3/2 and ± 1/2, located in alternating sites of a square lattice, with periodic boundary conditions as shown in Fig 1.

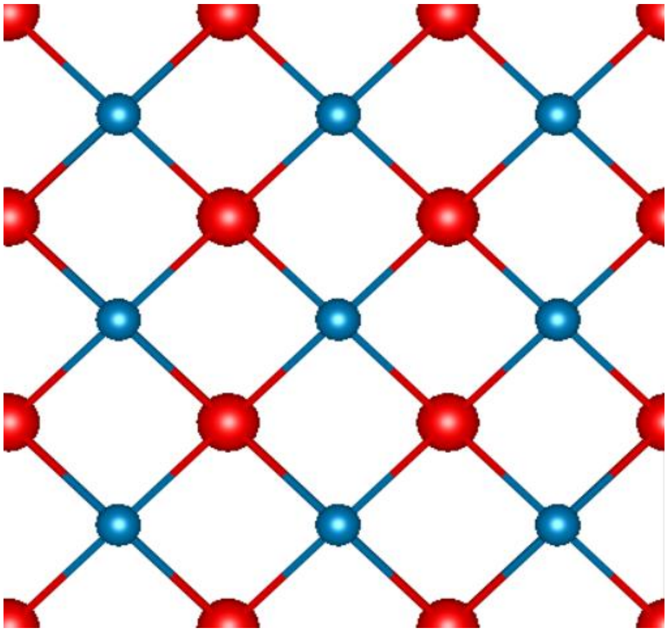

Fig 1: A section of the two-dimensional lattice systems. Gd (red ball) with spin $S_B=7/2$, and Cr (blue ball) with spin $S_A=3/2$.

The Hamiltonian of a ferrimagnetic mixed spin $\pm\frac{3}{2}$ and spin $\pm\frac{7}{2}$ square lattice Ising system in a zero magnetic field, can be written as [13],

$$H = -J\sum_{i,j} S_i^A S_j^B - D_A \sum_i (S_i^A)^2 - D_B \sum_j (S_j^B)^2 \tag{1}$$

Where [S_i^A, S_j^B] takes the values [$\pm\frac{3}{2}, \pm\frac{7}{2}$] respectively, J is a coupling constant between nearest neighbor, D_A is a magnetic anisotropy acting on Cl atoms, and D_B an acting on Gd atoms.

According to Maxwell-Boltzmann statistical the sublattice magnetization of the system is obtained [9].

$$m_A = \frac{1}{2}\frac{3\sinh(\frac{3}{2}\beta zJm_B) + e^{-2\beta D_A}\sinh(\frac{1}{2}\beta zJm_B)}{\cosh(\frac{3}{2}\beta zJm_B) + e^{-2\beta D_A}\cosh(\frac{1}{2}\beta zJm_B)} \tag{2}$$

$$m_B = \frac{1}{2}\frac{7\sinh(\frac{7}{2}\beta zJm_A) + 5e^{-6\beta D_B}\sinh(\frac{5}{2}\beta zJm_A) + 3e^{-10\beta D_B}\sinh(\frac{3}{2}\beta zJm_A) + e^{-12\beta D_B}\sinh(\frac{1}{2}\beta zJm_A)}{\cosh(\frac{7}{2}\beta zJm_A) + e^{-6\beta D_B}\cosh(\frac{5}{2}\beta zJm_A) + e^{-10\beta D_B}\cosh(\frac{3}{2}\beta zJm_A) + e^{-12\beta D_B}\cosh(\frac{1}{2}\beta zJm_A)} \tag{3}$$

3-Results:

The computed data on the thermal variations of the order parameters, which are the sublattice magnetizations, are shown in Figures (1-11) for selected values of the reduced crystal field strengths D_A and D_B. In Figure (1), when D_A is set to zero, the sublattice magnetization m_A (±3/2) decreases monotonically with increasing temperature, starting from its unique saturation value and vanishing at the critical temperature. Meanwhile, m_B(±7/2) exhibits seven saturation values with three hybrid states (-3, -2, -1), a behaviour similar to previous studies on (±7/2, ±3/2) systems[14,15]. In Figure (3.2), when the effect of the crystal field DA/|J| is introduced, the magnetization m_A (±3/2) shows three distinct saturation values, whereas m_B(±7/2) stabilizes into a single dominant state, highlighting the role of crystal field anisotropy in modifying the thermal properties of mixed-spin systems. The total magnetization, given by $M=(m_A+m_B)/2$, reveals different compensation behaviours, including L-, M-, N-, P-, Q-, R-, and S-type transitions, depending on the exchange interactions and crystal field parameters. At specific values of D_A and D_B, compensation points appear, where the sublattice magnetizations cancel each other, resulting in M=0. The system undergoes both first-order and second-order phase transitions, with abrupt changes observed at higher anisotropy values and smoother transitions occurring for moderate field strengths. These results are in agreement with previous studies on mixed-spin Ising systems but provide new insights into higher-spin (3/2, 7/2) configurations, particularly the presence of multiple intermediate magnetization plateaus, which suggest a more intricate spin arrangement compared to lower-spin models. In figure (3), the effect of the crystal field $D_A/|J|$ is evaluated here, three saturation values are recovered for ma (±3/2) while mb (±7/2) shows a unique saturation value.

In figures (5-11) L-, M-, N-, P-, Q-, R-, and S-type magnetic behaviors observed in the proposed system, similar to those obtained in [16] Notably, these results are in the absence of an external magnetic field. It is also worth to mention that area that is under the curve represent a ferromagnetic state of matter, while the area above the curve represents a paramagnetic state, hence the curve it self represent a second order phase transition from the ferromagnetic to the paramagnetic phase. One can notice that as the crystal fields of D_A and D_B increase the curie temperature (critical point) also increase as it represents the point at which the matter undergoes phase transition to the paramagnetic state.

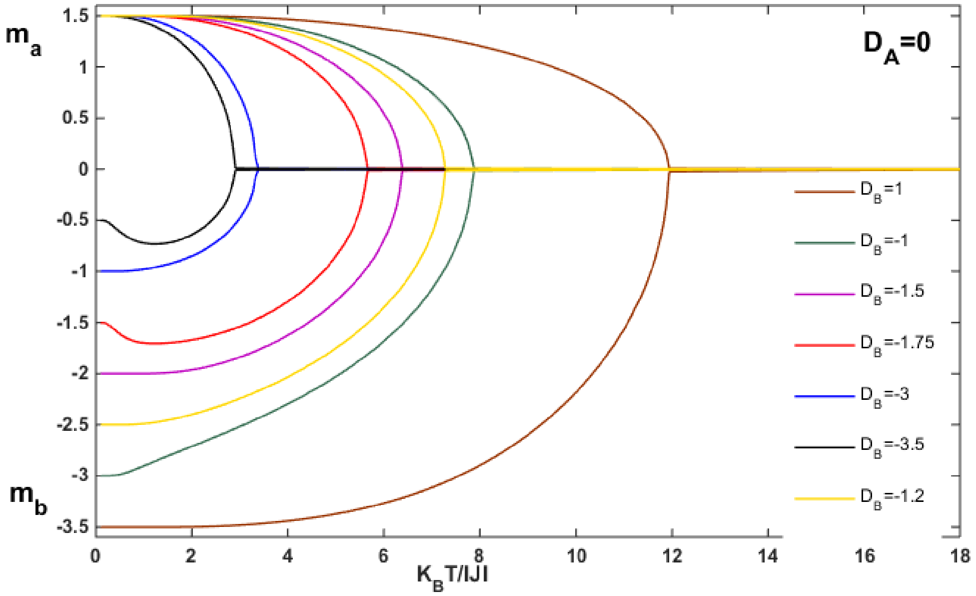

Fig 2: Thermal variation of the sublattice magnetizations m_a (Cr) and m_b (Gd) at $D_A/|J|$=0 and different values of $D_B/|J|$.

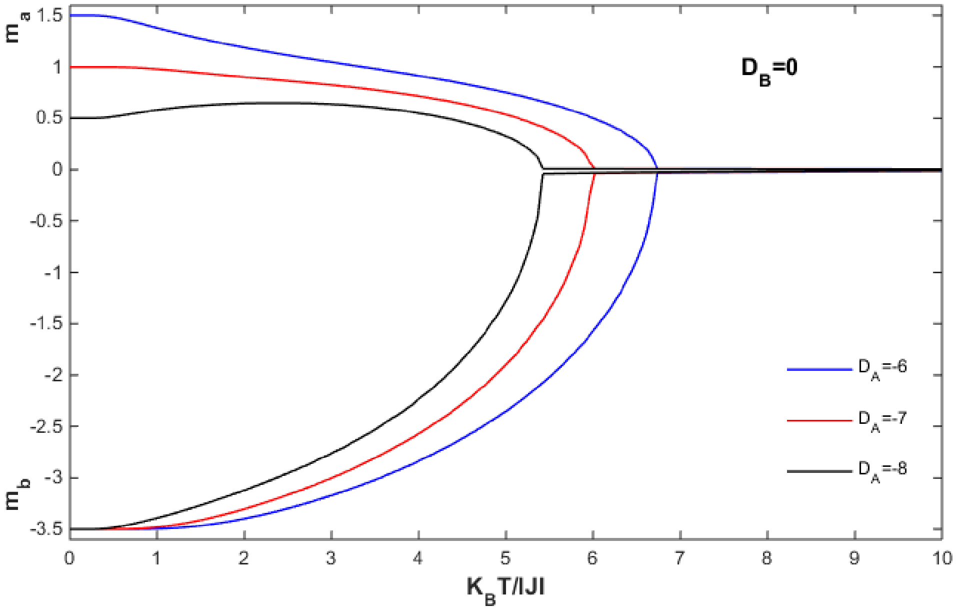

Fig 3: Thermal variation of the sublattice magnetizations m_a(Cr) and m_b (Gd) at $D_B/|J|$=0 and different values of $D_A/|J|$.

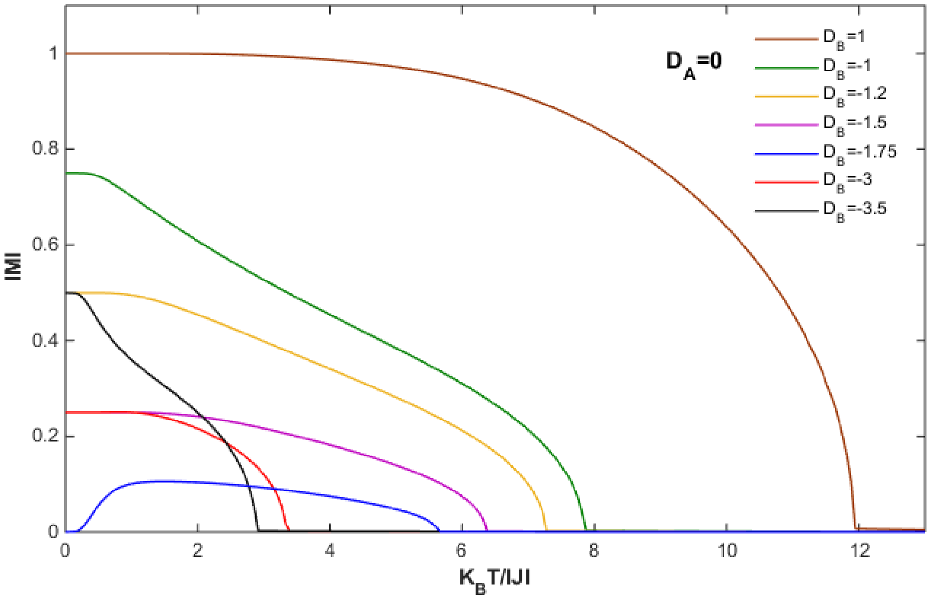

Fig 4: Thermal behavior of the absolute value of the total magnetization |M| for various values of the crystal field $D_B/|J|$when$D_A/|J| = 0$.

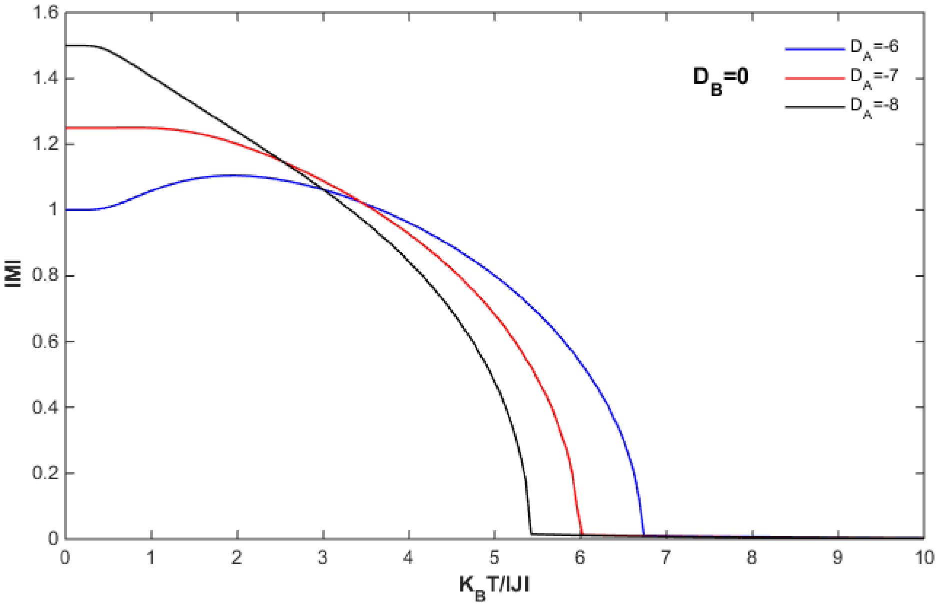

Fig4: Thermal behavior of the absolute value of the total magnetization |M| for various values of the crystal field $D_A/|J|$.when $D_B/|J| = 0$

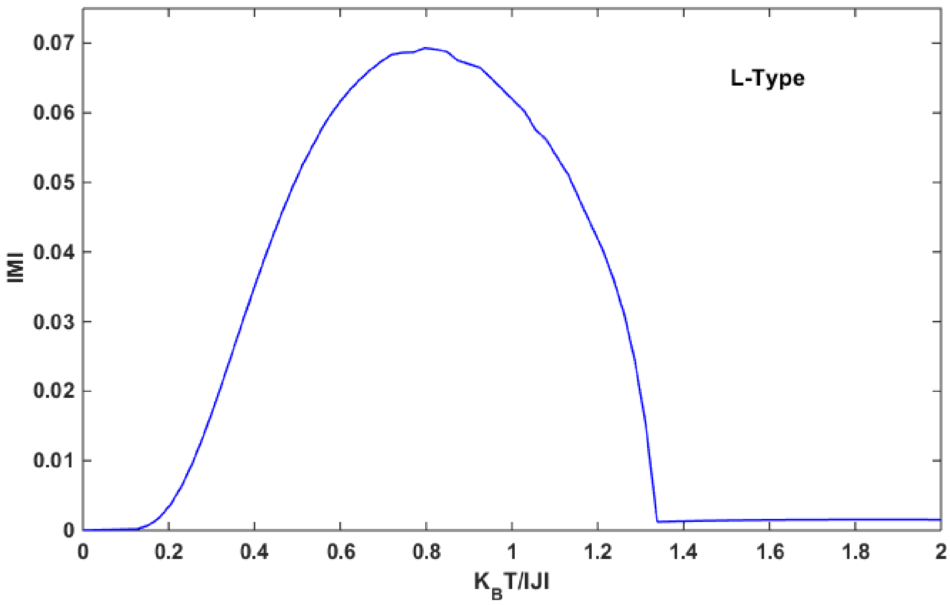

Fig 5: Temperature dependences of the absolute magnetization value |*M*| for the mixed ferrimagnet z = 4, when the values of $D_A/|J| = 1.5$, and $D_B/|J| = -0.5$.

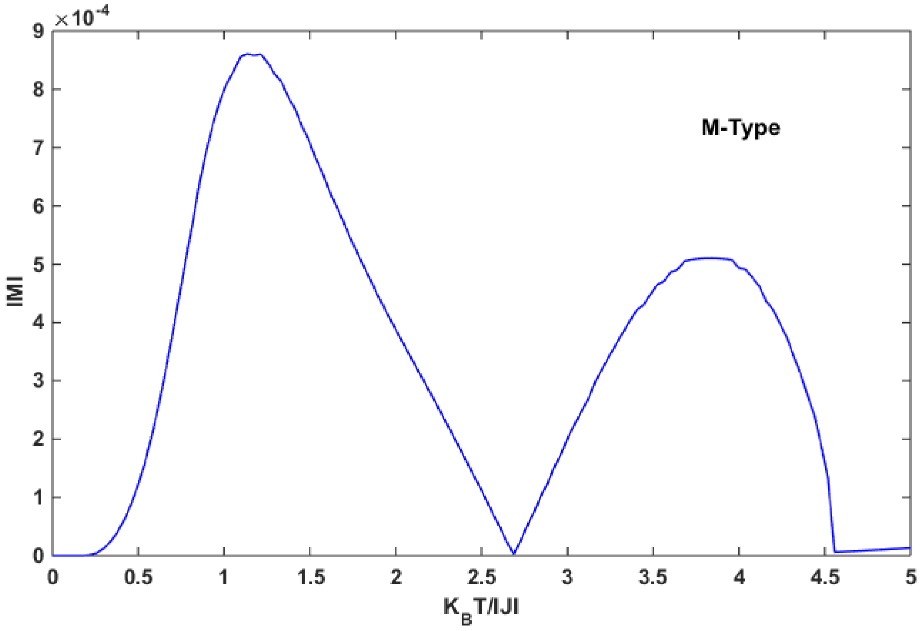

Fig 6: Temperature dependences of the absolute magnetization value |*M*| for the mixed ferrimagnet z = 4, when the values of $D_A/|J| = -0.5$, and $D_B/|J| = -1.999$.

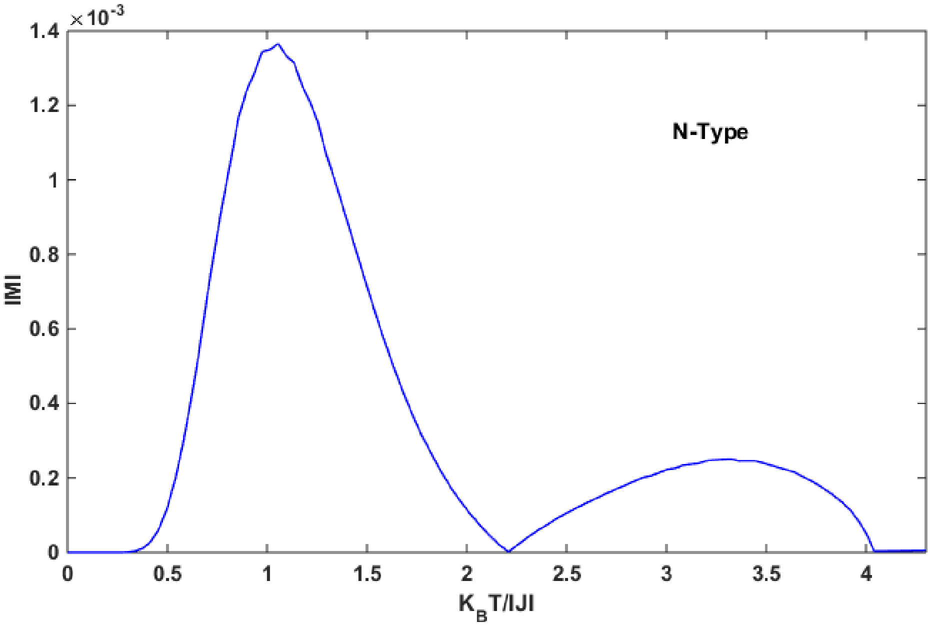

Fig 7: Temperature dependences of the absolute magnetization value $|M|$ for the mixed ferrimagnet z = 4, when the values of $D_A/|J| = -1.0$, and $D_B/ |J| = -2.0$.

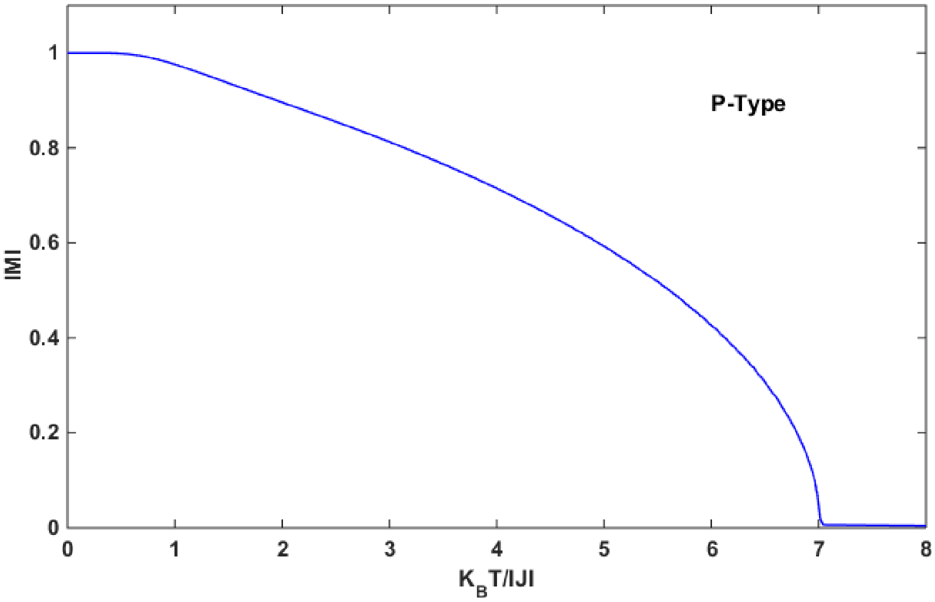

Fig 8: Temperature dependences of the absolute magnetization value $|M|$ for the mixed ferrimagnet z = 4, when the values of $D_A/|J| = -3.5$, and $D_B/ |J| = -0.5$.

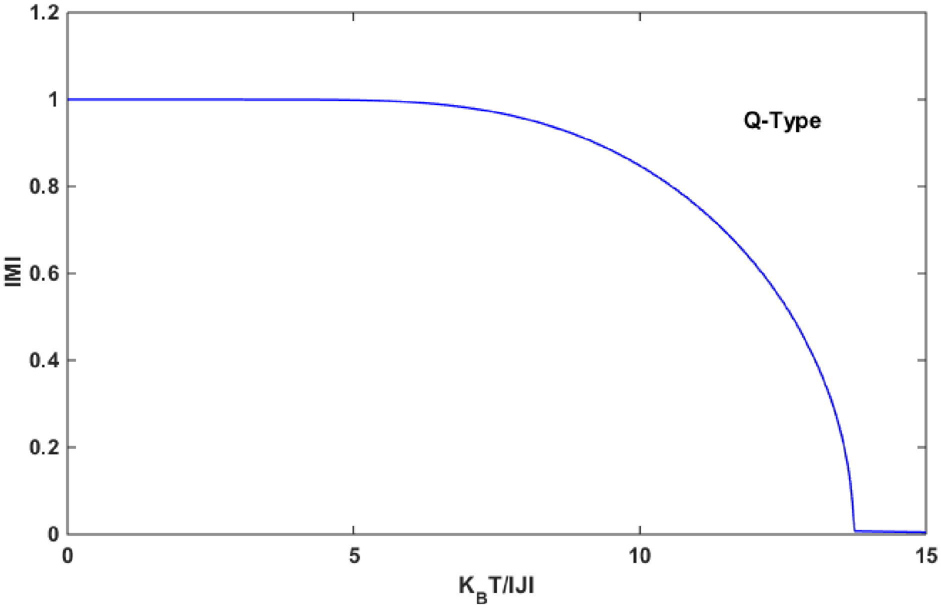

Fig 9: Temperature dependences of the absolute magnetization value |*M*| for the mixed ferrimagnet z = 4, when the values of $D_A/|J| = 2.0$, and $D_B/ |J| = 2.0$.

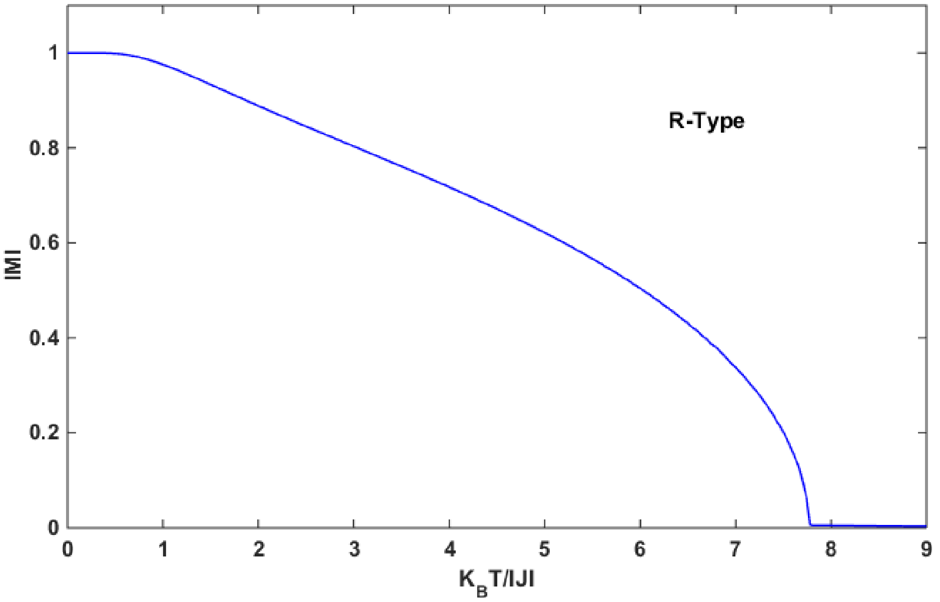

Fig 10: Temperature dependences of the total magnetization *M* for the mixed ferrimagnet z = 4, when the value of $D_A/|J|$= -2.5, and $D_B/ |J|$ = -0.5.

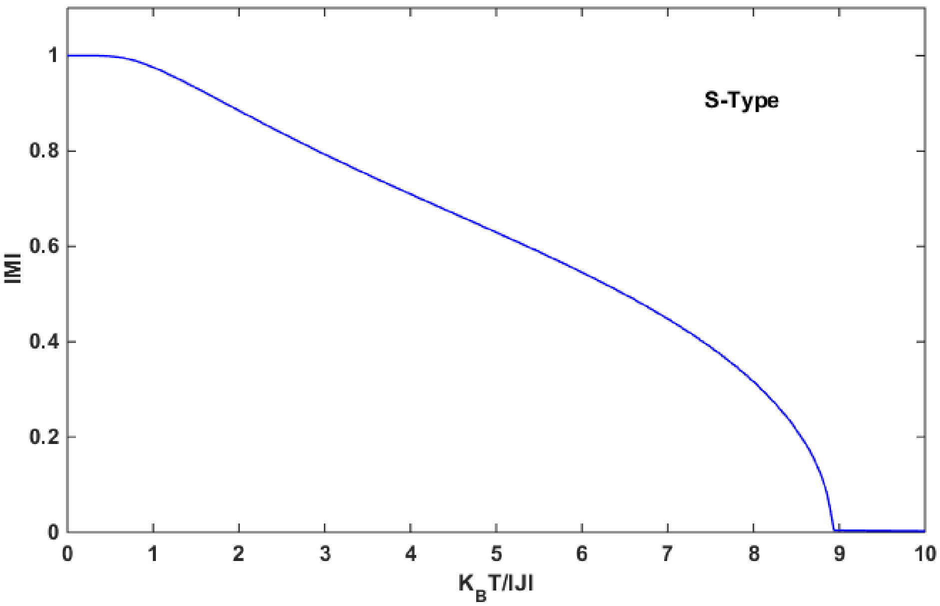

Fig 11: Temperature dependences of the total magnetization *M* for the mixed ferrimagnet z = 4, when the value of $D_A/|J|$= -0.5, and $D_B/ |J|$ = 0.5.

4 Conclusion:

In this study, we explored the magnetic properties and compensation behaviors of a mixed spin-(3/2,7/2) Ising ferrimagnetic system using the mean-field approximation. Our findings show that crystal field anisotropy plays a crucial role in shaping how sublattice and total magnetization evolve with temperature. We identified multiple compensation behaviors—L-, M-, N-, P-, Q-, R-, and S-type—each influenced by the balance between exchange interactions and crystal field effects.

One of the most interesting discoveries was the presence of multiple intermediate magnetization plateaus, which suggest a more intricate spin arrangement than what's typically seen in lower-spin systems. We also found that as the crystal field parameters D_A and D_B increase, the system's critical temperature rises, which could have implications for designing temperature-controlled magnetic devices.

These insights not only deepen our understanding of mixed-spin Ising models but also highlight their potential applications in spintronics and magnetic memory storage. Looking ahead, future studies could examine how external magnetic fields affect these behaviors or use Monte Carlo simulations to explore phase transitions and hysteresis effects in greater detail.

References:

[1] O. Kahn, C. Jay Martinez ,Spin-Transition Polymers: From Molecular Materials Toward Memory Devices.Science279,44-48(1998). DOI:10.1126/science.279.5347. 44.

[2] Leite, V., Godoy, M., Figueiredo, W.: Finite-size effects and compensation temperature of a ferrimagnetic small particle. Phys. Rev. B. 71, 094427 (2005).

[3] Svendsen, H., Overgaard, J., Chevallier, M.A., Collet, E., Chen, Y.S., Jensen, F., Iversen, B.B.: Photomagnetic Switching of Heterometallic Complexes[M(dmf)4(H2O)3(μ-CN)Fe(CN)5]·H2O (M=Nd, La, Gd, Y) Analyzed by SingleCrystal X-ray Diffraction and Ab Initio Theory. Chem. Eur. J. 16, 7215–7223 (2010).

[4] Zhang, Y., Duan, G., Sato, O., Gao, S.: Structures and magnetism of cyano-bridged grid-like two-dimensional 4f–3d arrays. J. Mater. Chem. 16, 2625–2634 (2006).

[5] Kodama, R.: Magnetic nanoparticles. J. Magn. Magn. Mater. 200, 359–372 (1999).

[6] Albayrak, E.: Mixed spin-3/2 and spin-5/2 Ising system on the Bethe lattice. Phys. Lett. A. 353, 121 (2006)

[7] Bahlagui, T., Bouda, H., El Kenz, A., Bahmad, L., Benyoussef, A.: Monte-Carlo simulation of compensation behavior for a mixed spin-5/2 and spin-7/2 Ising system with crystal field interaction. Superlattice. Microst. 110, 90–97 (2017)

[8] Jabar, A., Masrour, R.: Magnetic properties of mixed spin-5/2 and spin-2 Ising model on a decorated square lattice: a Monte Carlo simulation. Physica A. 515, 270–278 (2019).

[9] Mohamad, H.K., Zuhair, A. Ground-State Phase Diagram of a Mixed Spin-3/2 and Spin-7/2 Ising Model: A Study of Complex $[Cr(CN)_4(\mu\text{-}CN)_2Gd(H_2O)_4\text{-}(bpy)]_n.4nH_2O.1.5nbpy$. *J Supercond Nov Magn* **33**, 1481–1487 (2020). https://doi.org/10.1007/s10948-019-05352-w.

[10] H. Bouda, T. Bahlagui, L. Bahmad, R. Masrour, A. El Kenz, and A. Benyoussef, “Hysteresis Cycle and Magnetization Behaviors of a Mixed-Spin (7/2, 3/2) Ferrimagnetic Ising Model: Monte Carlo Investigation,” *J Supercond Nov Magn*, vol. 32, no. 8, pp. 2539–2550, Aug. 2019, doi: 10.1007/s10948-018-4981-4.

[11] A. El Antari et al., “Phase diagrams and hysteresis behavior of the mixed spin-7/2 and spin-1/2 Ising model,” *Physica A: Statistical Mechanics and its Applications*, vol. 578, Sep. 2021, doi: 10.1016/j.physa.2021.126113.

[12] Y. Kocakaplan and M. Keskin, “Hysteresis and compensation behaviors of spin-3/2 cylindrical Ising nanotube system,” *J Appl Phys*, vol. 116, no. 9, Sep. 2014, doi: 10.1063/1.4894509.

[13] Abed AA, Mohamad HK (2021) Magnetic characteristics of a mixed spin-3 and spin-7/2 Blume-Capel system for square and simple cubic lattices. Solid State Commun 338:114456. https://doi.org/10.1016/j.ssc.2021.114456

[14] De La Espriella, N., Karimou, M., & Buendía, G. M. (2021). Mixed Spin-(3/2, 7/2) Ising-Type Ferrimagnet: Monte Carlo–Mean Field Treatment. physica status solidi (b), 258(4), 2000536.

[15] Chakravorty, M., & Chowdhury, P. M. (2021). Crystal field effect on the magneto caloric properties of the mixed spin-7/2 and spin-3/2 3D-ising ferrimagnet: A Monte Carlo simulation. Journal of Magnetism and Magnetic Materials, 528, 167818.

[16] E. Kantar, B. Deviren, and M. Keskin, “Magnetic properties of mixed Ising nanoparticles with core-shell structure,” *Eur Phys J B*, vol. 86, no. 6, p. 253, Jun. 2013, doi: 10.1140/epjb/e2013-40080-9.

Al-Hamdaniya Journal for Pure Sciences, Vol:0, No:0, 2025 (43-56)

Mycobiome and Animal Health (Review)

[1]Hawraa F.H. Al-Abedi, [2]Suhail Gawdat Fadhil, [3]Israa Ibrahim Khalil, [4]Semaa F.H. Al-Abedi
[1,4]Department of Biology, Collage of Education for Pure Sciences, University of Al-Hamdaniya, Al- Hamdaniya, Nineveh, Iraq.
[2]Mosul Medical Technical Institute Northern Technical University (NTU).IRAQ.
[3]Department of Microbiology, College of Veterinary Medicine, University of Mosul, Mosul /Iraq.

E-mail: [1*] Hawraafaisal@uohamdaniya.edu.iq,[2]Suhail.gawdat@ntu.edu.iq , [3] israibrahim@uomosul.edu.iq, Semaa.f@uohamdanyia.edu.iq

Abstract:

The community of fungi that live in the gastrointestinal tract of animals, known as the animal gut mycobiota, is crucial to the health of the host. Animal gut mycobiota quantification is becoming more and more popular. The fungi that are likely to live in animal gastrointestinal tracts and the fungal species that are non-residents, including macrofungi, lichens, or plant symbionts/pathogens that can be consumed as part of the host's diet, are often not distinguished in studies on animal gut mycobiota. There is growing evidence that the gut "mycobiome," or intestinal fungus, are crucial for inflammation and host immunity. A more accurate knowledge of the causes and effects of variation in the composition of animal gut mycobiota should be made possible by taking into account the many sources and functions of fungi found in the gastrointestinal tract. In this review, we summarized the relationship between the gut mycobiome and health in animals, Role of fungal mycobiome as a member in the Ecosystem of animal's gut, classification and the importance in animal immunity with the Possibility of using them as alternative treatment options.

Keyword: Mycobiome, mycobiota, macrofungi.

1. Introduction

Our knowledge of the makeup and role of the mycobiome—the fungus community associated with the mucosal surfaces of humans and animals—has quickly increased during the last ten years. At birth, fungi invade different areas of the mucosal surface and are crucial for the immune system's development and homeostasis. Here, we examine the latest findings about the danimal mycobiome at several bodily locations, such as the oral cavity, the skin surface, the gastrointestinal (GI) tract, the respiratory tract, the urogenital tract, and the tumor tissues. Characterizing the interplay between the immune system and mycobiome, particularly in the GI tract, has taken a lot of research. We talk about mycobiome dysbiosis and how it affects the development of illnesses including alcoholic liver disease, inflammatory bowel disease, and systemic infections, highlighting the potential of mycobiome-focusing on life-threatening disease intervention strategies [1].

significantly to host health, which is why there is growing interest in quantifying the gut mycobiota of wild animals. This is because a mix of resident and non-resident gut fungi may make it difficult to identify processes associated with the authentic, resident gut mycobiota. A more accurate knowledge of the causes and effects of variation in wild animal guts should be made possible by taking into account the many sources and functions of fungi found in the gastrointestinal system of animals. composition of the mycobiota [2], [3]. Recent research examined fungal–bacterial interactions, fungal immunity promoting gut homeostasis, and the state of knowledge on the gut mycobiome in farmed animals. We will attempt to incorporate the mycobiome into the studies and research that addressed the relationship between fungi and animal immunity and health through this review.

2. Role of Fungi in animal Gut microbiome

The mycobiome is a horizontal iteration of a defined microbiome that includes all fungi (mycobiota). It is characterized by its quantitative and qualitative makeup, local or temporal variability, and the totality of interactions between its members and other components of the microbiome (bacteriome, virome), as well as, of course, with its environment. Modern software tools, techniques, and technologies created or modified to address fungal peculiarities are not equivalent to those offered for other microbiome iterations, such as bacteriome and virome.The complexity of any mycobiome may now be captured by metagenomic and culturomic techniques, with the former having a distinct advantage over the latter but still having significant drawbacks in its varied uses [4]. Numerous protists and communities of fungus, also known as the mycobiome, inhabit the bodies of humans and animals. The word "mycobiome" refers to the group of at least 60 fungal taxa that are present in the gastrointestinal tract (GIT) [5] . The fungal components of the microbiome are expected to affect host health and disease, just like the other components [6]. Through receptors like Dectin-1, fungi interact with innate immune cells in significant ways. According to research, colitis can result from disruption of the Dectin-1 receptor activity, possibly as a result of a loss of connections with host fungus. Obese patients also showed changes in their gut microbiota, which can be used to distinguish between metabolically healthy and unhealthy obesity [5]. Because of its relative richness, study on the oral mycobiome is also growing [5]. When it comes to identifying and verifying the components of this intestinal ecosystem, the mycobiota presents particular difficulties. Unlike bacteria, fungi are abundant in the environment and in a variety of dietary sources, such as cheese, beer, bread, wine, and airborne spores, but they are very rare in the gut. While the advent of deep sequencing techniques has given scientists the best chance to study the range of fungi that comprise the gastrointestinal (GI) "mycobiome", The data sets are vulnerable to accidental contamination from external sources and from other body surfaces (such as the face, hands, perspiration, etc.) due to the combination of low fungal DNA quantity in the gut and high dietary/environmental abundance. Many members of the bacterial population are reliant on the anaerobic environment that the gut provides, which significantly increases their likelihood of surviving in the intestines. They also outweigh fungal organisms. This is not the case for fungi, which are usually facultative anaerobes or tolerant of hypoxic conditions [5]. Delayed access to feed immediately post-hatch (PH) on the makeup of the mycobiome in chickens, since PH feed delay is frequently linked to subpar health outcomes. Chicken mycobiomes in each of the populations were distinct and changed over time. All mycobiomes were dominated by *Gibberella spp*., but *Aspergillus spp*., *Cladosporium spp*., *Sarocladium spp*., *Meyerozyma spp*., and *Penicillium spp*. were also abundant. During days one and two, penicillium was either completely missing or present in very little amounts in the cecal and ileal lumens, although it gradually increased. In luminal sites, Meyerozyma and Wickerhamomyces also grew over time. On the other hand, a number of extremely prevalent unclassified fungus declined following days one and two, underscoring the necessity for a better comprehension of fungal gut biology [7].With the exception of days one and two, there was no discernible difference in the mycobiomes of chicks fed during the first two days of PH compared to those not fed at that time. Mycobiome similarities between fed and unfed chicks at later timepoints imply that PH feeding delays do not have a permanent impact on the makeup of the mycobiome. Collectively, these findings establish the groundwork for further research on the mycobiome and indicate that the growth of fungal populations in the GIT is unlikely to be connected to the detrimental effects of delayed eating on health and productivity [8]. Fungi contribute to host health and development and are immunomodulatory .Mycobiome studies are currently focused on the fungi residing in healthy vs. diseased models, and more research has to go into the interactions between the myco- and microbiomes with the host (Figure 1) [9].

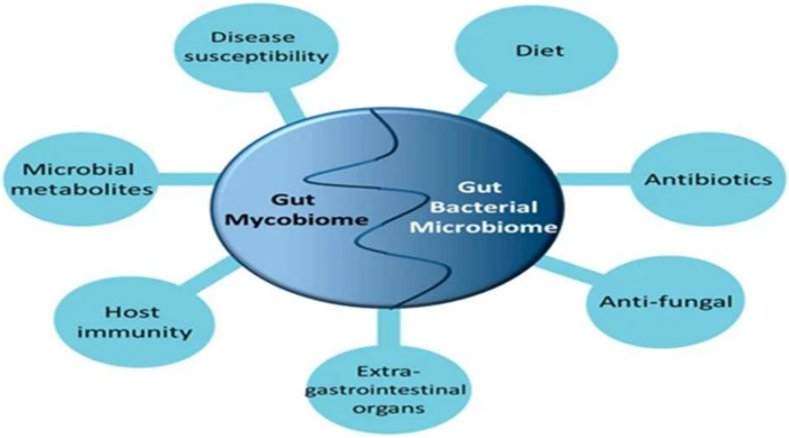

Figure 1. The multifaceted factors influencing gut microbiome and mycobiome interaction. Sam et al ., 2017.

3. Classification and Characterization of Mycobiome

Fungi are a diverse and widely distributed group of eukaryotes [10]. The estimated number of fungal species ranges from 2.2 to 3.8 million [11]. Until now, approximately 150,000 species of fungi have been described worldwide [12]. In previous studies, the classification of fungi primarily relied on their morphological characteristics. However, with the development of high-throughput sequencing technology, an increasing number of fungal genomes have been sequenced. In recent years, the taxonomic system of fungi has been updated using phylogenetic tree analyses based on whole-genome sequences. As a result, the number of phyla within the fungi kingdom has significantly increased from four to nine. Nevertheless, different classification systems resulted in different numbers of phyla [13].

The most prevalent fungi found in the intestinal tract are Ascomycota and Basidiomycota in all of humans, mice, pigs, and chickens [14]. Among them, Ascomycota is the largest group of fungi, including single-celled yeasts (Candida, Saccharomyces, etc.) and various filamentous molds (Aspergillus, Penicillium, etc.). Basidiomycota is closely related to Ascomycota and mainly consists of fungi with large sizes, and Malassezia is a common fungus in the gut [15].

In the gastrointestinal tract of most healthy people, there are ten genera which are considered as core fungal genera, including Candida (especially Candida albicans), Saccharomyces (particularly Saccharomyces cerevisiae), Penicillium, Aspergillus, Cryptococcus, Malassezia (particularly Malassezia restricta), Cladosporium, Galactomyces, Debaryomyces, and Trichosporon, following their abundances [16]. Fungal life cycles are complex and their morphological transformations can have an impact on adhesion, metabolic secretion, toxin secretion, and intestinal colonisation [17]. Compared to bacteria, fungi show a lower amount and abundance in the gut. However, they play important roles in host physiology. Gut fungi take part in the metabolism of nutrients and the production of enzymes [18]. Candida and yeast are the most common fungi in the gut. Among species in Candida, C. albicans belongs to an opportunistic pathogen. Overgrowth of this fungus is often associated with a variety of diseases, especially in immunocompromised individuals.It also plays a significant role in host immunity as a form of antigen exposure [19]. Confounding redundancies are also widespread in fungal databases, since many fungus contain sexual and asexual forms and are consequently misdiagnosed as two separate taxa assigned even to different families [20].

4. Gut Mycobiota impact host health

The complex communities of commensal microbes (viruses, fungus, bacteria, and protozoa) that are found in all animals are known as the microbiota, and they can number anywhere from hundreds to thousands of species [21]. The bacterial communities that live in the gastrointestinal system are arguably the most significant and extensively researched aspect of host-associated microbiota [22] . Numerous studies have found that gut bacteria can affect host health in a variety of ways, such as by digesting otherwise indigestible meals to provide vital vitamins and metabolites [22], [23].

Perhaps as a result of the hostile environment of the (vertebrate) stomach, the direct contribution of food material to the apparent makeup of gut bacteria is rarely investigated. [24], is expected to kill many ingested microbes such that the composition of the gut microbiota should reflect the dynamics of the authentic resident bacteria. The following are the main justifications for using animal gut mycobiota analyses: (1) The number of fungal cells in the animal intestine is far lower than that of bacteria. (Huffnagle and Noverr 2013) and (2) many animals consume fungi. As a result, there is a greater chance of a significantly lower signal to noise ratio (i.e., a higher contribution of allochthonous material) in gut mycobiota analyses as opposed to gut bacterial analyses [25] .

Due to technological restrictions, there are currently few research on the gut mycobiome of farm animals; nevertheless, the topic has advanced recently with the advent of high throughput sequencing techniques. Fungi have been shown to have intricate interactions in the gut environment, despite ongoing difficulties with DNA separation, primer design, PCR settings, and database accuracy.

Moreover, the gut bacteriome exhibits α-diversity and succession, whereas fungi do not, indicating a different colonization process [26]. Over the past few years, mycologists' research has finally proven that the fungal community and its hitherto underappreciated members are essential parts of the microbiome. The importance of commensal fungal microbes and other microbiota members in their relationship with the human host is now indisputable.Current studies are characterizing the fungal community and offering fresh perspectives on the biological processes by which the human host, the microbiome, their genomes (metagenome), and metabolites (metabolome) interact in multiple directions to eventually impact health and/or disease states [27] .

Mycobiome also plays a significant role in host immunity as a form of antigen exposure [28] . The two most prevalent fungi in the stomach are Candida and yeast. Of the species of Candida, Candida albicans is an opportunistic pathogen. Numerous illnesses are frequently linked to this fungus's overgrowth, particularly in immunocompromised people. For instance, a recent study discovered that patients with ulcerative colitis had far higher levels of Candida albicans in their colonic mucosa. By releasing the peptide toxin candida lysin, some strains can increase intestinal inflammation. This toxin led to a high level of the pro-inflammatory cytokine interleukin (IL)-1β and damaged macrophage immune cells [29] [30]. But according to a another study, patients with Crohn's disease had abnormal inflammatory CD4 T cell responses that were influenced by the intestine commensal fungus Candida albicans [13], [32]. The various strains of Candida albicans should be responsible for this disparate outcome. Additionally, additional Candida species can potentially have effects that are resistant to illness. An encouraging discovery revealed that people with inflammatory bowel disease have higher levels of Candida in their gut flora [33]. Among them, Candida metapsilosis M2006B has been identified as an agonist that can metabolise farnitol X receptor to relieve colitis in mice [33] . To our knowledge, current studies have indicated that yeast shows numerous benefits in the gut [34]. For instance, yeast in the gut plays a role in regulating host immune homeostasis [35]. Interestingly, yeast can also promote the gut barrier function and enhance the mouse social behaviours. A novel finding has suggested that yeast residing in the gut mucosa can protect the gut barrier by inducing Th cells to secrete IL-22 that has a role in anti-infection. It can also affect host behaviours through the IL-17 signalling pathway in neuronal cells [36], [30].

5. The interaction of mycobiome with other Ecosystem microorganisms in animal

Because infectious diseases are so common, researchers are now concentrating on the host-pathogen relationship in order to create new management and prevention techniques. Recent developments in next-generation sequencing technology have provided insight into the composition and function of microbiomes in various habitats and hosts. Animal microbiome (Ecosystem), including bacteria (bacteriome), fungi (mycobiome), archaea (archaeome), and viruses (virome) has become a growing area of research and increasingly recognized as an important driver of animal health and productivity. Therefore, the development of techniques to enhance animal health and productivity while lowering the incidence of disease requires an understanding of the complexity of animal microbiomes and their interactions with the host [37].

Although they are statistically smaller than bacteriomes and viromes, the animal mycobiome and archaeome have both lately been identified as important elements in animal health [37]. It has been demonstrated that the mycobiome and archaeome of animals are made up of different lineages, are extensively dispersed, and exhibit patterns unique to different body sites. Animal mycobiomes and archaeomes have not received as much attention as they should because of difficulties with primer design, bioinformatics, maintaining a well-curated database, and having less DNA than bacteriomes. It has been discovered that, in spite of these difficulties, the animal mycobiome and archaeome interact intricately with other animal microbiome members throughout the creation of ecosystems and affect host health. Additionally, studies have demonstrated that the mycobiome and archaeome are more amenable to manipulation by environmental factors, including nutrition, than the bacteriome, which makes them a prime option for dietary treatments aimed at promoting the health and growth of animals [38]. It is necessary to conduct more research on the processes via which the animal mycobiome and archaeome interact with other microbiome members [37].

Numerous abiotic and biotic factors, including management techniques, dietary composition, physiological circumstances, stress, and disease states, can influence animal microbiomes and their relationships with hosts [39]. As a result, altering the microbiomes of animals at various phases of the production cycle is a compelling idea for the animal production industry and has been proposed as a potential substitute for the use of antibiotics in the livestock sector. Data from [40]. showed that outdoor access periods with access to natural dietary sources increase the richness and diversity of cecal microbiota in chickens as well as increase the biosynthesis of micronutrients involved in vital cell processes. This study offered fresh perspectives on how nutrition and environmental conditions affect the gastrointestinal microbial communities' developmental dynamics and forecasted metabolic processes in broiler chickens raised in a free-range environment [40].

Modification of particular animal microbiome members can optimize critical metabolic pathways and enhance host phenotypes and productivity, according to a new field of study in medicine and agriculture [41]. Fecal microbiota transplantation is a unique and underutilized method that has been widely employed in veterinary medicine to improve host-mediated microbiome selection and modify microbiome composition [42].

By artificially transferring the microbiome from healthy individuals, fecal microbiota transplants attempt to enhance host function. Ramírez et al., showed that giving fecal microbiota transplant to day-of-hatch chicks from healthy adults result in significantly higher body mass of birds and decreased residual feed intake, implying enhanced feed efficiency at 6 weeks of age [43], [44].According to the findings, early-life microbiome transplants may be a major step toward microbiome-focused sustainable agriculture since they alter market-relevant phenotypes in chicken. Candida, Trichosporon, and Aspergillus were the dominating species in our earlier study (not yet published), which revealed that the mycobiota in the broiler gut was primarily made up of Ascomycota and Basidiomycota, which were considerably more prevalent in the middle and later stages of life. Furthermore, a recent study on the mycobiota of chickens revealed that Gibberella was among the most prevalent genera [45].

In ruminants, research on mycobiota has primarily focused on fungi in the rumen, with special attention given to anaerobic fungi belonging to the phylum Neocallimastigomycota [46]. Amplicon sequencing in Ujimqin sheep revealed that the large intestine was largely colonized by Dothideomycetes and Leotiomycetes, while the stomach and small intestine were preferentially colonized by Neocallimastigomycetes and Sordariomycetes, respectively. Meanwhile, Cryptococcus was significantly enriched in the small intestine, and Sporormiaceae was significantly dominant in the large intestine [47].

Caprinae animals (e.g., goats, sheep, and antelopes) display species polymorphism. They can survive in a variety of climates, geographies, heights, and feeding conditions. In these environments, ruminants' ability to digest fiber and absorb nutrients is greatly impacted by temperature, vegetation, and water(Figure 2). [48].

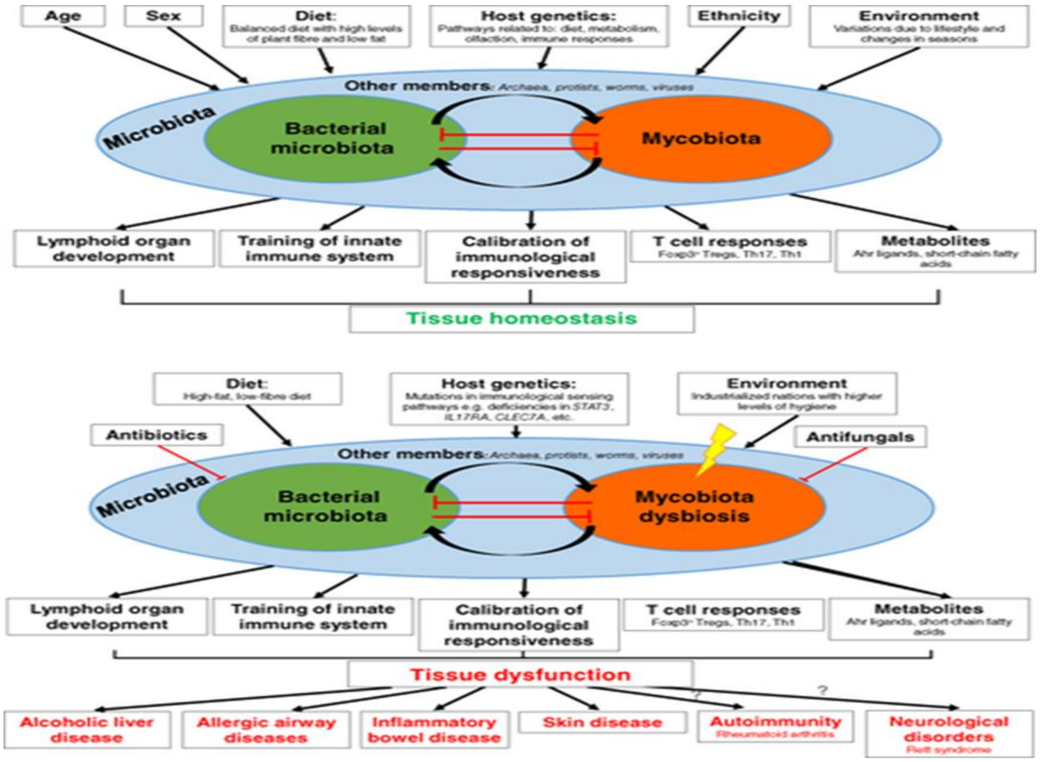

Figure 2: Graphical Abstract: The consortium of symbiont fungi on mammalian mucosal surfaces, collectively known as the mycobiota, exerts substantial effects on human health. Perturbations to the mycobiota due to host or environmental factors can disrupt these complex and dynamic interactions and potentially contribute to disease [49].

6. Identification of Mycobiome

It is still mostly unclear how much each component contributes to the commensalism-pathogenicity flip in some fungi, including Candida, and how much each component affects the mycobiome's makeup and functionality. Therefore, more research is needed to fully understand the mycobiome in relation to animal health and disease. The first step in achieving this goal is to develop consensus methodologies in mycobiome research that will allow for accurate isolation and identification through comparative analysis across various studies.

6.1. Culture-dependent methods

Growing fungi on solid or liquid media treated with antibiotics is the gold standard for fungal identification. The species is assessed by examining the shape of colonies or actively proliferating cells. This is the clear-cut way to find live fungi, even though a failed culture doesn't always mean there aren't any at all [50], [51]. Unfortunately, many fungi are not cultivable, hence it is currently not possible to define the viable component of mycobiotas using just culture-dependent approaches. Moreover, these methods are poor at detecting low-abundance species, unless one has a target species in mind and a strategy to selectively enrich for it. It should come as no surprise that prior mycobiome research employing culture-dependent techniques consistently revealed a much lower level of variety than analyses that were independent of culture [52], identifying less than 30% of the fungal species reported in the human gut [53]. However, these techniques continue to be very useful for evaluating phenotypes both within and between species, including growth, cell shape, drug resistance, and other characteristics related to host adaptability [54].

6.2. Culture-independent methods and their challenges

By detecting fungus directly from their genomic DNA or RNA content, culture-independent approaches avoid the issues mentioned above, but they also come with a new set of limitations and difficulties.

6.2.1. Fungal viability cannot be unequivocally established

Since extracellular nucleic acids from dead cells might survive in the environment and cannot be distinguished from those in living organisms, it is crucial to note that sequencing techniques are ultimately agnostic of the viability status of the microbial cells under analysis. Sequencing techniques, particularly DNA-based methods, have the potential to inflate the kind and quantity of viable species found in microbial communities if live microorganisms are not selectively recognized. [55]. The number and kind of viable species found in microbial communities may be inflated by sequencing techniques, particularly DNA-based ones, if living bacteria are not selectively discovered [56].

6.2.2. Efficient genomic content isolation

To determine the actual diversity and abundance of fungal communities, all sequencing-based techniques need to extract nucleic acids in an efficient and objective manner. Although techniques for extracting genetic content have been established for bacteria in microbiome investigations, they are typically ineffective for fungi because of their hard cell walls, which make it difficult to lyse them. A recent study assessing DNA extraction techniques from saliva samples showed that the technique used had a significant impact on the variety of fungus, in contrast to their bacterial counterparts [57]. Based on our experiences and other comparative studies of DNA extraction methods [58]. For efficient genetic content recovery, at least one more bead-beating step is necessary to guarantee mechanical destruction of fungal cell walls [58], [59]. [60]. Fungi make up a little but significant portion of the microbiome, ranging from 0.03% in the gut to over 10% on the skin, making this particularly crucial for mycobiota research [61] Furthermore, metagenomic methods are too costly for large-scale investigations since they need a sufficient sequencing depth to produce an accurate fungal signature [62].

7. Therapeutic Potential of Mycobiome and Future direction

Current mycobiome research focuses on characterizing whole fungal communities that live in both healthy and diseased persons, and it is beginning to show that changes in the abundance of particular mycobiota members are linked to a number of diseases [63], [64]. The majority of host-microbe associations are the consequence of several intricate and dynamic microbe-microbe and microbe-host interactions where the host environment is always changing, even though these top-down methods are useful for determining simple host-microbe interactions. Due of these difficulties, efforts have been made to better understand these relationships utilizing bottom-up methods by studying paired interactions in vivo by monocolonization in germ-free animals or in vitro using model microorganisms.Understanding pairwise competitive and cooperation outcomes [65], [66]. Will allow for the prediction of survival when these pairs are placed in within the context of a larger number of species [67]. However, research on fungal monocolonization can also uncover novel and surprising facets of fungal biology: Unlike the morphologically diverse population seen in mice treated with antibiotics, *C. albicans* in monocolonized mice has been shown to take on a commensal-like yeast-cell morphology [68].

Conclusion:

It is anticipated that quantifying the variety and function of the gut mycobiota would improve our comprehension of the mechanisms influencing wild animals' fitness and health. The need for clarification on the definition of an authentic gut mycobiota as determined by standard high-throughput amplicon sequencing surveys is highlighted by the frequent presence of dietary material and/or noteworthy plant symbionts and plant diseases in wild animal gut mycobiota communities. When analyzing the gut mycobiota of animals, it is evident that a deeper consideration of the ecology and life history of the fungi is necessary. Compared to the mycobiota of humans, there are fewer data available for animals.

Reference:

1. Y. Fan, L. Wu, B. Zhai. The mycobiome: interactions with host and implications in diseases. Current Opinion in Microbiology. Vol 75:102361 2023. DOI: 10.1016/j.mib.2023.102361.

2. A. Lavrinienko, T. Scholier, S. T. Bates, A. N. M. Ph. C. Watts. Defining gut mycobiota for wild animals: a need for caution in assigning authentic resident fungal taxa. Animal Microbiome. Vol 3 (75). 2021.

3. S.M. Hird. Evolutionary biology needs wild microbiomes. Front Microbiol.;8:725. 2017. https://doi.org/10.3389/fmicb.2017.00725.

4. J.C. Clemente, L.K. Ursell, L.W. Parfrey, R Knight. The impact of the gut microbiota on human health: an integrative view. Cell 148:1258–70. 2012. https://doi.org/10.1016/J.CELL.2012.01.035.

5. A. Zipperer, M.C. Konnerth, C. Laux, A. Berscheid, D. Janek, C. Weidenmaier, et al. Human commensals producing a novel antibiotic impair pathogen colonization. Nature.535:511–6. 2016.https://doi.org/10.1038/nature18634.

7. D.E. Beasley, A.M. Koltz, J.E. Lambert, N. Fierer, RR Dunn. The evolution of stomach acidity and its relevance to the human microbiome. PLoS ONE. 10: 2015. e0134116. https://doi.org/10.1371/JOURNAL.PONE.0134116.
8. G.B. Huffnagle, M.C. Noverr. The emerging world of the fungal microbiome. Trends Microbiol. 21:334–41. 2013. https://doi.org/10.1016/j.tim.2013.04.002.
9. K. L. Summers & A. M. Arfken. The Gut Mycobiome and Animal Health. Book series. The Microbiomes of Humans, Animals, Plants, and the Environment Chapter. First Online. 85–125. 2022.
10. N El-Jurdi, M. A. Ghannoum. The Mycobiome: Impact on Health and Disease States. ASM Journals. Microbiology Spectrum. Vol 5(3). 2017. https://doi.org/10.1128/microbiolspec.funk-0045-2016.
11. I. Hamad, S. Ranque, E. I. Azhar, M. Yasir, A. A. Jiman-Fatani, H. Tissot-Dupont, F. Bittar. Culturomics and amplicon-based metagenomic approaches for the study of fungal population in human gut microbiota. Scientific Reports, 7(1): 16788. 2017. 10.1038/s41598-017-17132-4.
12. I.I. Khalil. Fungal infections in Cyprinus carpio fish in Mosul city, Iraq, Veterinary Practitioner 22 (2): 205-211. 2021. https://cabidigitallibrary.org by 45.143.30.44, on 01/17/25
13. I. Hamad, D. Raoult, F. Bittar. Repertory of eukaryotes (eukaryome) in the human gastrointestinal tract: Taxonomy and detection methods. Parasite Immunology, 38(1): 12–36. 2016. 10.1111/pim.12284.
14. F. Strati, M. Di Paola, I. Stefanini, D. Albanese, L. Rizzetto, P. Lionetti, C. De Filippo. Age and gender affect the composition of fungal population of the human gastrointestinal tract. Frontiers in Microbiology, 7, 1227. 2016. 10.3389/fmicb.2016.01227.
15. P. Carini, P. J. Marsden, J. W. Leff, E. E. Morgan, M. S. Strickland, & N. Fierer. Relic DNA is abundant in soil and obscures estimates of soil microbial diversity. Nature Microbiology, 2: 16242. 2016. 10.1038/nmicrobiol.2016.242.
16. A. Vesty, K. Biswas, M. W. Taylor, K. Gear, & R. G. Douglas. Evaluating the impact of DNA extraction method on the representation of human oral bacterial and fungal communities. PLoS One, 12(1), e0169877. 2017. 10.1371/journal.pone.0169877.
17. C. E. Huseyin, R. C. Rubio, O. O'Sullivan, P. D. Cotter, & P. D. Scanlan. The fungal frontier: A comparative analysis of methods used in the study of the human gut mycobiome. Frontiers in Microbiology, 8. 2017.1432 10.3389/fmicb.2017.01432.
18. Human Microbiome Project Consortium (2012). A framework for human microbiome research. Nature, 486(7402), 215–221. 10.1038/nature11209.
19. Y. Belkaid & J. A. Segre. Dialogue between skin microbiota and immunity. Science, 346(6212), 954–959. 2014.10.1126/science.1260144.
20. F. Cottier, K. G. Srinivasan, M. Yurieva, W. Liao, M. Poidinger, F. Zolezzi & N. Pavelka. Advantages of meta-total RNA sequencing (MeTRS) over shotgun metagenomics and

amplicon-based sequencing in the profiling of complex microbial communities. NPJ Biofilms Microbiomes, 4, 2. 2018.10.1038/s41522-017-0046-x.

21. C. M. Liu, S. Kachur, M. G. Dwan, A. G. Abraham, M. Aziz, P. R. Hsueh, L. B. Price. FungiQuant: A broad-coverage fungal quantitative real-time PCR assay. BMC Microbiology, 12. 2012. 255 10.1186/1471-2180-12-255.
22. C. L. Schoch, K. A. Seifert, Huhndorf, S. , Robert, V. , Spouge, J. L. , Levesque, C. A. Fungal Barcoding Consortium . (2012). Nuclear ribosomal internal transcribed spacer (ITS) region as a universal DNA barcode marker for fungi. Proceedings of the National Academy of Sciences of the United States of America, 109(16), 6241–6246. 10.1073/pnas.1117018109.
23. K. Schubert, J. Z. Groenewald, U. Braun, J. Dijksterhuis, M. Starink, C. F. Hill, P.W. Crous. Biodiversity in the Cladosporium herbarum complex (Davidiellaceae, Capnodiales), with standardisation of methods for Cladosporium taxonomy and diagnostics. Studies in Mycology. 58. 2007. 105–156. 10.3114/sim.2007.58.05.
24. L. Kiss. Limits of nuclear ribosomal DNA internal transcribed spacer (ITS) sequences as species barcodes for fungi. Proceedings of the National Academy of Sciences of the United States of America, 109(27). 2012. E1811. doi: 10.1073/pnas.1207143109.
25. C. L. Schoch, K. A. Seifert, S. Huhndorf, V. Robert, J. L. Spouge,C. A. Levesque. Nuclear ribosomal internal transcribed spacer (ITS) region as a universal DNA barcode marker for fungi. Proceedings of the National Academy of Sciences of the United States of America, 109(16), 6241–6246. 2012. doi: 10.1073/pnas.1117018109.
26. J. Tang, I. D. Iliev, J. Brown, D. M. Underhill, & V. A. Funari. Mycobiome: Approaches to analysis of intestinal fungi. Journal of Immunological Methods. 421, 112–121. 2015.doi.10.1016/j.jim.2015.04.004.
27. F. Cottier, A. S. M. Tan, M. Yurieva, W. Liao, J. Lum, M. Poidinge, N. Pavelka. The transcriptional response of Candida albicans to weak organic acids, carbon source, and MIG1 inactivation unveils a role for HGT16 in mediating the fungistatic effect of acetic acid. G3 (Bethesda), 7(11), 3597–3604. 2017.doi. 10.1534/g3.117.300238.
28. B. Halwachs, N. Madhusudhan, R. Krause, R. H. Nilsson, C. Moissl-Eichinger, C. Hogenauer, G. Gorkiewicz. Critical issues in mycobiota analysis. Frontiers in Microbiology, 8.180. 2017. https://doi.org/10.3389/fmicb.2017.00180.
29. E. Pruesse, C. Quast, K. Knittel, B. M. Fuchs, W. Ludwig, J. Peplies & F. O. Glockner. SILVA: A comprehensive online resource for quality checked and aligned ribosomal RNA sequence data compatible with ARB. Nucleic Acids Research, 35(21), 7188–7196. 2017. doi: 10.1093/nar/gkm864. Epub 2007 Oct 18.
30. K. Abarenkov, N. R. Henrik, K. H. Larsson, I. J. Alexander, U. Eberhardt, S. Erland, U. Koljalg. The UNITE database for molecular identification of fungi—Recent updates and future perspectives. New Phytologist, 186(2), 281–285. 2010.doi.10.1111/j.1469-8137.2009.03160.x.
31. D. S. Hibbett, M. Binder, J. F. Bischoff, M. Blackwell, P. F. Cannon, O. E. Eriksson, N. Zhang. A higher-level phylogenetic classification of the fungi. Mycological Research, 111(Pt. 5), 509–547. 2007.doi.10.1016/j.mycres.2007.03.004.

32. J. Gore, H. Youk & A. van Oudenaarden. Snowdrift game dynamics and facultative cheating in yeast. Nature, 459(7244), 253–256. 2009.doi.10.1038/nature07921.
33. J. Friedman, L. M. Higgins & J. Gore. Community structure follows simple assembly rules in microbial microcosms. Nature Ecology and Evolution, 1(5), 109. 2017.doi. 10.1038/s41559-017-0109.
34. L. Bohm, S. Torsin, S. H. Tint, M. T. Eckstein, T. Ludwig, & J. C. Perez. The yeast form of the fungus Candida albicans promotes persistence in the gut of gnotobiotic mice. PLoS Pathogens, 13(10), e1006699. 2017.doi.10.1371/journal.ppat.1006699.
35. E.K. Manousos and V. Aristea. Chapter 3 - Myc(et)obiome: The Big Uncle in the Family. Microbiomics. Microbiomics. 29-52. 2020. https://doi.org/10.1016/B978-0-12-816664-2.00003-7.
36. D. F. William, I.H. Gao, D. I. Iliyan. Gut mycobiota under scrutiny: fungal symbionts or environmental transients? Current Opinion in Microbiology. Vol (50):79-86. 2019 https://doi.org/10.1016/j.mib.2019.09.010.
37. P. D. Cary, L. S. Katie, M. A. Ann, D. Nadia, C. Atul, F. F. Juli, S. Lori, P. W. Monika. Temporal dynamics of the chicken mycobiome. Front Physiol 15:13:1057810. 2022. doi: 10.3389/fphys.2022.1057810.
38. T. B. E Van, V.K. Pettersen, M.W. Gutierrez, I. Laforest-Lapointe, N.G. Jendzjowsky, J.B.Cavin, F.A. Vicentini, C.M. Keenan, H.R. Ramay, J. Samara, W.K. MacNaughton, R.J.A. Wilson, M.M. Kelly, K.D. McCoy, K.A. Sharkey, M.C. Arrieta.. Intestinal fungi are causally implicated in microbiome assembly and immune development in mice. Nat Commun 11. 2020. doi: 10.1038/s41467-020-16431-1.
39. H. S. Qi, W. C. Matthew and Y. A. C. Louis (). The Fungal Mycobiome and Its Interaction with Gut Bacteria in the Host. Int. J. Mol. Sci. 18(2), 330. 2017.https://doi.org/10.3390/ijms18020330.
40. M. A. Naranjo-Ortiz & T. Gabaldón. Fungal evolution: Major ecological adaptations and evolutionary transitions. Biological Reviews, 94(4), 1443–1476. 2019. https://doi.org/10.1111/brv.12510.
41. D. L Hawksworth, & R. Lücking. Fungal diversity revisited: 2.2 to 3.8 million species. Microbiology Spectrum, 5(4). 2017.https://doi.org/10.1128/microbiolspec.FUNK-0052-2016.
42. L. Tedersoo, S. Sánchez-Ramírez., U. Kõljalg, M. Bahram, M. Döring, D. Schigel, T. May, M. Ryberg & K. Abarenkov. High-level classification of the fungi and a tool for evolutionary ecological analyses. Fungal Diversity, 90(1), 135–159. 2018. https://doi.org/10.1007/s13225-018-0401-0.
43. J. Hu, J. Chen, Q. Hou, X. Xu, J. Ren, L. Ma, & X. Yan. Core-predominant gut fungus Kazachstania slooffiae promotes intestinal epithelial glycolysis via lysine desuccinylation in pigs. Microbiome, 11(1), 31. 2023.https://doi.org/10.1186/s40168-023-01468-3.
44. A. K. Nash, T. A. Auchtung, M. C. Wong, D. P. Smith, J. R. Gesell, M. C. Ross, C. J. Stewart, G. A. Metcalf, D. M. Muzny, R. A. Gibbs, N. J. Ajami & J. F. Petrosino. The gut mycobiome of the Human Microbiome Project healthy cohort. Microbiome, 5(1), 153. 2017.https://doi.org/10.1186/s40168-017-0373-4.

45. M. L. Richard, & H. Sokol. The gut mycobiota: Insights into analysis, environmental interactions and role in gastrointestinal diseases. Nature Reviews Gastroenterology & Hepatology, 16(6), 331–345. 2019. https://doi.org/10.1038/s41575-019-0121-2.
46. K. S. Ost, & J. L. Round. Commensal fungi in intestinal health and disease. Nature Reviews Gastroenterology & Hepatology, 20, 723–734. 2023.https://doi.org/10.1038/s41575-023-00816-w.
47. C. Hoffmann, S. Dollive, S. Grunberg, J. Chen, H. Li, G. D. Wu, J. D. Lewis, & F. D. Bushman (). Archaea and fungi of the human gut microbiome: Correlations with diet and bacterial residents. PLoS One, 8(6), e66019. 2013 https://doi.org/10.1371/journal.pone.0066019.
48. D. M. Underhill, & I. D. Iliev. The mycobiota: Interactions between commensal fungi and the host immune system. Nature Reviews Immunology, 14(6), 405–416. 2014.https://doi.org/10.1038/nri3684.
49. G. R. Martini, E. Tikhonova, E. Rosati, M. B. DeCelie, L. K. Sievers, F. Tran, M. Lessing, A. Bergfeld, S. Hinz, S. Nikolaus, J. Kümpers, A. Matysiak, P. Hofmann, C. Saggau, S. Schneiders, A. K. Kamps, G. Jacobs, W. Lieb, J. Maul, P. Bacher. Selection of cross-reactive T cells by commensal and food-derived yeasts drives cytotoxic T(H)1 cell responses in Crohn's disease. Nature Medicine, 29(10), 2602–2614. 2023 https://doi.org/10.1038/s41591-023-02556-5.
50. X. Huo, D. Li, F. Wu, S. Li, Y. Qiao, C. Wang, Y. Wang, C. Zhou, L. Sun, Z. Luan, Q. Yan, J. Wang, Y. Zhang, T. Zhao, Y. An, B. Zhang, X. Tian, Z. Yu, & X. Ma. Cultivated human intestinal fungus Candida metapsilosis M2006B attenuates colitis by secreting acyclic sesquiterpenoids as FXR agonists. Gut, 71(11), 2205–2217. 2022https://doi.org/10.1136/gutjnl-2021-325413.
51. T. T. Jiang, T. Y. Shao, W. X. G. Ang, J. M. Kinder, L. H. Turner, G. Pham, J. Whitt, , T. Alenghat & S. S. Way. Commensal fungi recapitulate the protective benefits of intestinal bacteria. Cell Host & Microbe, 22(6), 809–816.e4. 2017. https://doi.org/10.1016/j.chom.2017.10.013.
52. I. Doron, I. Leonardi, X. V. Li, W. D. Fiers, A. Semon, M. Bialt-DeCelie, M. Migaud, I. H. Gao, W. Y. Lin, T. Kusakabe, A. Puel, & I. D. Iliev. Human gut mycobiota tune immunity via CARD9-dependent induction of anti-fungal IgG antibodies. Cell, 184(4), 1017–1031.e14. 2021. https://doi.org/10.1016/j.cell.2021.01.016.
53. I. Leonardi, I. H. Gao, W. Y. Lin, M. Allen, X. V. Li, W. D. Fiers, M. B. De Celie, G. G. Putze, R. K. Yantiss, M. Johncilla, Colak, D., & Iliev, I. D.. Mucosal fungi promote gut barrier function and social behavior via Type 17 immunity. Cell, 185(5), 831–846.e14. 2022.https://doi.org/10.1016/j.cell.2022.01.017.
54. Wei G (2024). Insights into gut fungi in pigs: A comprehensive review. Journal of animal physiology and animal nutrition. Vol 109 (1):96-112. https://doi.org/10.1111/jpn.14036.
55. Z. Mohamed, E. Ahmed, Alharthi. Abdulrahman, A Mohamed. Editorial: The role of the bacteriome, mycobiome, archaeome and virome in animal health and disease. Front Vet Sci.10;9:1130187. 2023. doi: 10.3389/fvets.2022.113018.

56. M. Zeineldin, A. Megahed, B. Blair, B. Aldridge, J. Lowe. Metagenomic analysis of the fecal archaeome in suckling piglets following perinatal tulathromycin metaphylaxis. Animals. 11:1825. 202110.3390/ani11061825.
57. K.L. Summers, J.F. Frey, T.G. Ramsay, A.M. Arfken. The piglet mycobiome during the weaning transition: A pilot study. J Anim Sci 97:2889–900. 2019 10.1093/jas/skz182.
58. Al-abedi H.F.H, K. Zaker, K. Mumtaz, A. Adil. Fluorescence Microscopy Detection of Cryptococcus Neoformans Isolated From Chicken and Pet Birds Dropping Samples in Mosul Province. Egyptian Journal of Veterinary Sciences. Vol. 55(1): 41-47. 2024.
59. Al-abedi H.F.H.and I. K. Israa. Molecular Detection of Virulence Factor Genes in Candida parapsilosis Isolated from Subclinical Mastitis Goats and Antifungal Susceptibility in Mosul Province. Volume 56 (1):185-193. 2025.
60. Al-abedi H.F.H., I.K. Israa, Al-Abedi S.F.H. Molecular detection of Virulence Factor Genes in Candida albicans Isolated from the Oral Cavity of Local Chicken and Antifungal Susceptibility in Mosul Province. Al-Kitab Journal for Pure Sciences. Vol 8 (2). 2024https://doi.org/10.32441/10.32441/kjps.08.02.
61. R.S. Peixoto, D.M. Harkins, K.E. Nelson. Advances in microbiome research for animal health. Ann Rev Anim Biosci. 9:289–311. 202110.1146/annurev-animal-091020-075907.
62. V. Lorena, C. Lorena, D. Ludovico, D. G. Brian, P.Antonino, L. Francesca, F.M. Lucia, F. Alessandro, B. Luca. An Outdoor Access Period Improves Chicken Cecal Microbiota and Potentially Increases Micronutrient Biosynthesis. Front. Vet. Sci., Veterinary Infectious Diseases. Vol 9. 2022 https://doi.org/10.3389/fvets.2022.90452.
63. M.H. Kogut. The effect of microbiome modulation on the intestinal health of poultry. Anim Feed Sci Technol. 250:32–40. 2019.10.1016/j.anifeedsci.2018.10.008.
64. M.C. Niederwerder. Fecal microbiota transplantation as a tool to treat and reduce susceptibility to disease in animals. Vet Immunol Immunopathol. 206:65–72. 2018 10.1016/j.vetimm.2018.11.002.
65. A. R. Gustavo, K. Jitendra, V. Isabella, I. G. Arkadiy, E. B. Mark, A. C. Nelson, G.C .Fernando, E. A. Samuel, B. O. Brian. Cecal Microbial Hydrogen Cycling Potential Is Linked to Feed Efficiency Phenotypes in Chickens. Front. Vet. Sci., Veterinary Infectious Diseases. Vol 9. 2022 https://doi.org/10.3389/fvets.2022.904698.
66. K. Robinson, Q. Yang, S. Stewart, M.A. Whitmore, G. Zhang. Biogeography, succession, and origin of the chicken intestinal mycobiome. Microbiome 10:55. 2022.
67. M.M.Y. Elghandour, A. Khusro, M.J. Adegbeye, Z. Tan, S.H. Abu Hafsa, R. Greiner, E.A Anele, U.Y. Ugbogu, A.Z.M. Salem. Dynamic role of single-celled fungi in ruminal microbial ecology and activities. J Appl Microbiol 128:950–965. 2020.
68. J. Yang, Z. Yu, B. Wang, F. Ndayisenga. Gut region induces gastrointestinal microbiota community shift in Ujimqin sheep (Ovis aries): from a multi-domain perspective. Environ Microbiol 23:7603–7616. 2021.

Al-Hamdaniya Journal for Pure Sciences, Vol: 0, No: 0, 2025 (9-20)

Study of the chemical and physical properties of hydroxyapatite and polyvinylpyrrolidone (HA/PAP) composite

Abdulrahman I. Ahmed[1,*], Ahmed T. Abdulhameed[1]

[1]Department of Physics, Education College for Pure Science, University of Al-Hamdaniya, Mosul, Iraq.

E-mail *: a.i.ahmed@uohamdaniya.edu.iq

Abstract :

Porous composite materials based on polyvinylpyrrolidone and hydroxyapatite (Ca10(PO4)x(CO3)y(OH)) were fabricated using foaming followed by freeze-drying and were fabricated ex situ. The materials were studied using scanning electron microscopy, swelling technique, EPR spectroscopy and transmission electron microscopy. The porosity of the materials was in the range of 70-90% under physiological conditions (pH 7.4, temperature 37 °C). The biocompatibility of the resulting materials was investigated in vitro. The developed materials were promising for the treatment of damaged bones and soft tissues.

Keyword: polyvinylpyrrolidone, tricalcium phosphate, hydroxyapatite, EPR spectroscopy, SEM, TEM.

1. Introduction

One of the urgent tasks of modern medical materials science is the creation of biodegradable polymer-based membrane materials. Currently, the development of porous films for dentistry is the most common and important topic [1-3]. These materials can act as a reservoir for the local delivery of drugs to the affected area. The advantages of these dosage forms lie in their duration of action and the precision of the active ingredient dosage. Their use in dentistry allows for the treatment of diseases associated with inflammatory periodontal diseases [4]. Films are an effective means of delivering drugs across the mucous membrane. Using such a material, it is possible to regulate the release kinetics of active ingredients and prolong the therapeutic effect by combining different dosage forms in a carrier (film) [5]. The choice of polyvinylpyrrolidone (PVP (polyvinylpyrrolidone) is valued for its excellent biocompatibility with body tissues and its ability to be reabsorbed into body fluids [6] without releasing toxic degradation products. In the 1960s, aqueous solutions of PVP were used as a blood substitute [7]. Due to PVP's high solubility in aqueous solutions, it is difficult to use as a polymer matrix in medical materials. To reduce the rate of biosynthesis, partial crosslinking of PVP is necessary. A method for partial crosslinking PVP under gamma radiation has been described [8]. However, this crosslinking method requires expensive equipment. A simpler approach involves using polymer mixtures of PVP with polymers that can be easily crosslinked by adding non-toxic reagents. Sodium alginate is used as a second polymer in these mixtures [9].

Sodium alginate is a naturally occurring polysaccharide obtained from brown algae. It is a heteropolymer composed of polyuronic acid residues (D-mannuronic and L-guluronic acids are present in varying proportions, depending on the specific algae species. Adding divalent, trivalent, or tetravalent metal salts to sodium alginate solution forms insoluble alginates of these metals, which are often used for the partial bonding of alginate-containing materials [10]. Polyvinylpyrrolidone mixtures with alginate [11] are known to be used as wound dressings.

A large bone defect can be filled with microspheres. They adapt better to the irregularity of the bone defect than cement. The microspheres support alginate andβ-TCP and HA microglobules replaced by alginate/Sr form bone and are replaced by bone tissue without any allergic or inflammatory reactions [12,13].

Polymer and calcium phosphate compounds are also used to deliver the targeted drug via gradual release [12]. For example, alginate-Self-hardening β-TCP, being biodegradable, is able to release an antimicrobial drug during absorption [13], in addition to alginate-gelatin-HA [14].

One of the important properties of composite materials for bone regeneration is not only the preservation of cell proliferation, but also osteoconduction, i.e., the ability of bone cells to adhere to and proliferate on the implant surface [15]. The material contains an alginate (1%) - gelatin (2.5%) composition.HA (0.5%) on a high index for this property [16].

The incorporation of calcium phosphate into the polymer matrix is promising from the perspective of imparting hemostatic properties to the material. The aim of this work is to obtain polymer-based composite materials fromPVP and sodium alginate containing hydroxyapatite carbonate (Ca10(PO4)x(CO3)y(OH)2, CHA), and studying their microstructure, strength and biological behavior in the laboratory.

2. Preparation Materials and methods Measurement:

To obtain composite membrane materials fromFor PVP and HA, in situ synthesis of HA was carried out in a 3 wt% solution of PVP and sodium alginate according to reaction (1). The reaction mixture was then poured onto a polyethylene substrate and dried at room temperature and 80–100% humidity. To increase the stability of the films in aqueous solutions, they were partially crosslinked by immersing the dried film in a 5% solution of iron(III) salicylate coordination compound. The HA content in the polymer matrix was in the range of 1–10 wt%. To obtain bulk porous composites, a mixture of PVP and HA was prepared, synthesized off-site according to reaction (2), and heat-treated at 400 °C to remove byproducts. The resulting mixture was then blended with the addition of 0.001% sodium dodecyl sulfate using an overhead mixer at a speed of 1500 rpm. The foam mass was squeezed through a syringe into a solution of ferrous salicylate (3+). After 5 minutes the bulk material was removed from the solution, frozen at -10°C, and then dried in an LS-1000 freeze dryer.

$$10Ca(NO3)2 + x(NH4)2HPO4 + y(NH4)2CO3 + 8NH4OH \rightarrow Ca10(PO4)x(CO3)y(OH)2 + 2NH4NO3 + H2O \qquad (1)$$

$10CaO + x(NH_4)_2HPO_4 + y(NH_4)_2CO_3 + 2H_2O \rightarrow Ca_{10}(PO_4)_x(CO_3)_y(OH)_2 + (2x+2y)NH_3\uparrow$ (2)

The degree of swelling of membranes made from polyvinylpyrrolidone mixtures with sodium alginate was determined by the change in mass when immersed in a physiological solution. The porosity of the bulk materials was determined using a porosity meter.TriStar 3000.

The fine structure of the membranes was studied using a scanning electron microscope (SEM) using the Tescan Vega II scanning electron microscope (Czech Republic).

Electron magnetic resonance studies were conducted (EPR) was performed on Bruker Elexsys E580 (X-band, ν = 9.61 GHz) and E680 (W-band, ν = 94 GHz) spectrometers, which are also equipped with a helium purification chiller and a thermostat system to achieve specific temperatures in the range of 6 to 300 K. In pulsed mode, the Hahn sequence π/2–τ–π–τ–(electron spin resonance (ESE)) was used, where the duration π/2 = 64 ns and τ = 250 ns. Electron magnetic resonance spectra were obtained by measuring the integrated density of electron magnetic resonance during continuous scanning of the magnetic field B0. The photomagnetic centers were excited by continuous laser irradiation at wavelengths λ = 266 nm and λ = 355 nm. To create stable radiation centers, the samples were exposed at room temperature to X-ray radiation for one hour on a URS-55 device with an absorption dose of 15 kGy.

3. Results and discussion:

The ability of the membranes to swell was determined by the change in the mass of the membranes when immersed in a physiological solution (Table 1).

Table 1. Degree of swelling of interconnected membranes immersed in saline solution

Samples	Time to reach maximum swelling, min	Swelling degree, wt.%	Swelling degree, wt.% a day later
Alginate	18	294	281
Alginate + CHA	20	300	292
Alginate-PVP (2:1)	15	311	266
Alginate- PVP (2:1)+CHA	15	280	257
Alginate-PVP (1:1)	3	350	291
Alginate- PVP (1:1)+CHA	5	300	284

Related films have similar swelling values; insertionPVP increases swelling. Adding CHA, even at a 5% concentration, reduces the films' ability to swell due to the compression of the material, as can be seen in Figure 2. The decrease in the mass of the swollen samples after one day can be explained by the relaxation of the polymer chains and the release of a certain amount of fluid into the surrounding solution volume. Adding CHA affects this process in the same way as swelling.

With the introductionIn the alginate matrix, the degree of film swelling is slightly reduced, while with the introduction of DCPD into the PVP-alginate mixed matrix, the degree of swelling increases compared to the original matrix. Cross-linking of the film with iron salicylate leads to a decrease in swelling. This can be explained by the increased number of bonds between the large polymer molecules, making it more difficult for water molecules to penetrate the cells between the PVP and alginate molecules. The swelling of the membranes is likely related to the filling of the pore space with fluid.

The fine structure of the mixed film fromPVP and sodium alginate are porous (Figure 1), with pore sizes ranging from 10 to over 100 micrometers, and interpore wall thicknesses of 5-10 micrometers.

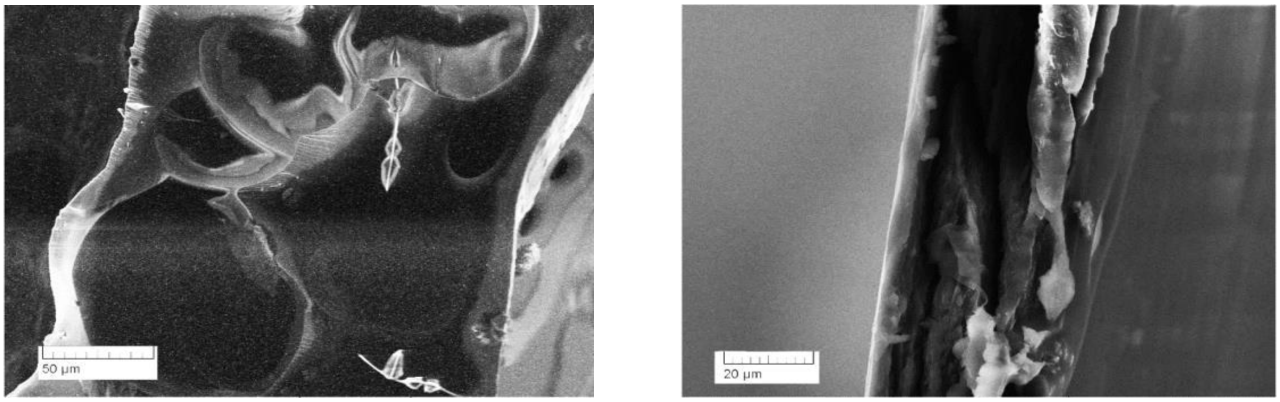

(a) (b)

Figure 1. Scanning electron microscope image of: a) A section of mixed film fromPVP-alginate; b) Mixed film of PVP-alginate with CHA crystals

The film structure represents polymer walls containingHA (Figure 1b). The size of HA particles ranges from several micrometers to 15-20 micrometers, and the pore size within the film is 4-5 micrometers.

Regarding the samples (In HA and HA-PVP, the EPR signal is not observed due to the absence of magnetic centers (PCs) in the material structure. Photoirradiation or X-ray irradiation of the samples allows for the formation of photo-induced or radioactively induced magnetic centers with a spin S = ½, which belong to the stable free radical (FR) class. The samples under study contain a synthesis byproduct—ammonium nitrate—which, after irradiation, transforms into the magnetic state NO2-3. The EPR spectrum of the nitrogen radical in HA-PVP is presented in Figure 3. This SR has previously been shown to be a suitable spin probe for studying the local environment of magnetic centers [17]. Figure 2 illustrates the dependence of the EPR spectra on the PVP concentration, where, with increasing polymer content, there is an increase in the ultrafine reaction constant (HFC) A(2A).⊥(Pure HA - 67.7 g, HA-0.07 PVP - 68.7 g, HA-0.69 PVP - 70 g; 2A||: Pure HA - 134.4 g, HA-0.07 PVP - 135.5 g, HA-0.69 PVP - 136.5 g). Calculations of the contributions to the HFC value show that the increase in constant A occurred mainly due to the isotropic component (Fermi reaction), the mechanism of which is related to the presence of electron density of FP on the 14N nitrogen nucleus with nuclear spin I = 1. Apparently, the insulating surface of PVP concentrates/distorts the electron cloud of near-surface nitrogen radicals on the 14N nitrogen nucleus. Other (additional) explanations for the observed effect: 1) For HA-PVP, we observe near-surface nitrogen radicals with a distorted electron cloud, which, due to the polymer shell, do not recombine under the influence of environmental ions; 2) A change in the degree of polarization of the near-surface radicals due to PVP. The continuous increase in the HFC constant and the distribution of the value A|| indicate an increase in the thickness of the polymer layer around the HA particles. Monitoring the dimensions of the coating is crucial for medical purposes because the time required for PVP reabsorption/dissolution during targeted drug delivery and the prolongation of its therapeutic effect depend on this. Therefore, the EPR method is capable of monitoring the extent to which the polymer coating covers the HA particles. The absence of amplitude for the central HFC component (mI = 0) indicates that any changes in the HFS lines are solely due to the constant A.

In this work, the dynamic properties of nitrogen radicals in the range were also studied.X at room temperature (Table 2). No significant changes were found in the longitudinal relaxation times T1 and transverse relaxation times T2, indicating that PVP has no effect on the crystal structure of HA.

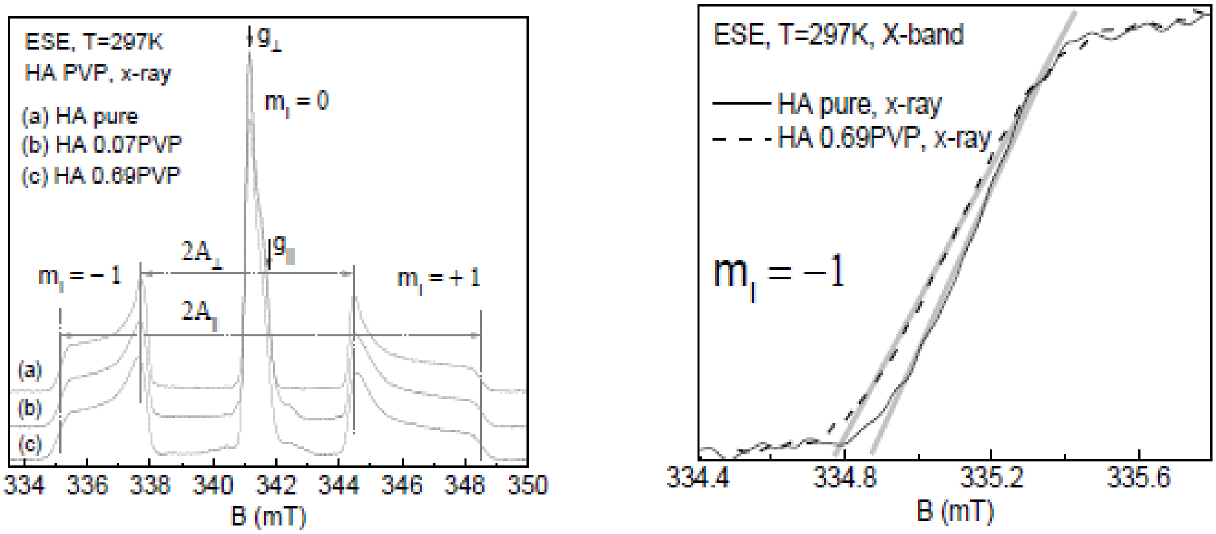

Figure 2. On the left – illustrates the dependence of spectraEPR for HA on PVP concentration, on the right - shows the distribution or dispersion of the change in coefficient A|| with PVP concentration.

Table 2. Nitrogen radical relaxation properties depending on concentrationPVP in HA for the value B0, corresponding to g⊥In SpectraEPR (Figure 2).

Samples	T1 (µsec)	T2 (µsec)
HA	28.5	3
HA 0.007 PVP	26	3.13
HA 0.69 PVP	27.6	3.2

Figure (3) illustrates the effect of ionization (X-rays) and laser radiation at a specific wavelength.λ = 266 nm and λ = 355 nm on the W-band high-frequency (HF) EPR spectra of PVP, HA, and HA-0.069PVP. Depending on the radiation wavelength, different paramagnetic and photoinduced radicals are formed, each with different activation energies. These centers may have a different local environment from other neighboring centers, offering prospects for further study of photoinduced radicals using nuclear electron-double resonance methods. For comparison, samples were chosen after X-ray irradiation, as in this case, the EPR signals are the most intense and suitable for analysis.

Spectra differHA and PVP differ significantly from each other because they are generated by different types of free radicals. However, the lack of significant difference between the HA and HA-PVP samples indicates that the polymer fully bonded to the HA surface. Furthermore, after X-ray exposure, no radiation or photoinduced PC compounds were detected in the polymer. As with the EPR in the X-band (Table 3), no effect of PVP was observed on the measured relaxation times T1 and T2 of the paramagnetic centers observed in HA and HA-PVP.

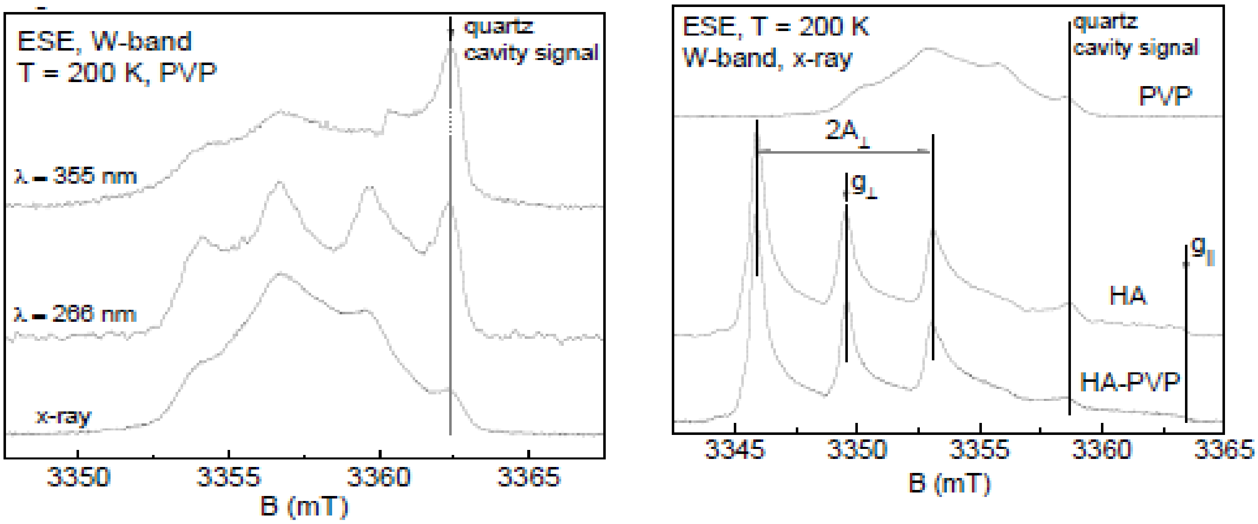

Figure 3. On the left – a pleasant viewEPR for PVP depending on the wavelength of light radiation; on the right are the EPR spectra of different compounds.

A laboratory experiment showed that a composite material ofPVP-alginates containing HA, synthesized on-site, exhibited acute cytotoxicity. The cytotoxicity of this HA-containing compound is clearly related to the degradation of the byproduct of the HA formation reaction (see Reaction 1) – ammonium nitrate – in an aqueous environment. The degradation of ammonium nitrate occurs according to Equation (3):

$$NH4NO3 + H2O \leftrightarrow NH3 + HNO3 \qquad (3)$$

The nitric acid released during hydrolysis leads to cell death, giving the substance cytotoxicity.

According to the results of transmission electron microscopy studiesTEM found that the shape of the particles that make up the samples is round as in Figure (3).

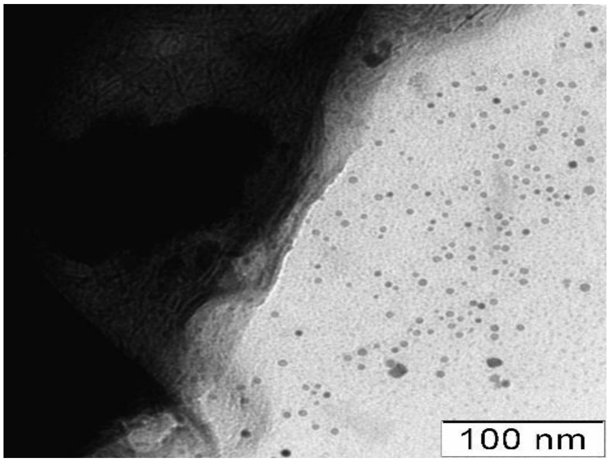

Figure 4. ImageTEM for HA composite materials with PVP.

Table 3 shows the results of determining the dimensional properties of materials obtained by different methods.

Table 3. Powder particle size characteristics obtained from compounds HA-PVP after heat treatment (T = 400°C) determined by TEM and X-ray powder diffraction.

No.	PVP content, g	HA/PVP ratio	Specific surface area, m^2/g	CSR, nm	TEM particle size, nm
1	0	–	18	32	35
2	0.69	14.5	19	18	30
3	1.38	7.2	37	20	33
4	2.75	3.6	17	18	45

It was observed that the particle size of the composite materials obtained from the dataTEM significantly exceeds the value of CSR. It was also shown that the microstructure of the composite materialHA with uniform PVP as in Figure 5, represented by irregularly shaped lamellar crystals.

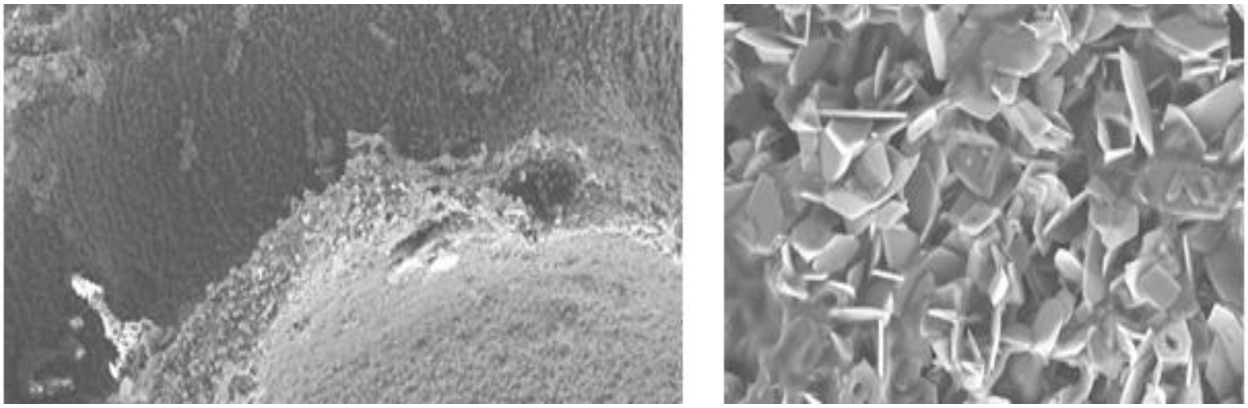

Figure 5. The microscopic structure of composite materialsHA with PVP.

Figure (5) indicates that the additionThe conversion of PVP to HA reduces the degree of crystallinity, thereby increasing the surface roughness of the resulting composite. The importance of controlling surface roughness in biomedical applications, particularly in bone implants, has been demonstrated.

The results showed a strong correlation between increased surface roughness and bone formation and resorption. It also contributes to the balance of bone components in bone grafting. Furthermore, it was found that osteoblast differentiation and osteocellular proliferation depend on surface roughness, thus establishing a strong relationship between surface roughness and bone-to-implant bonding.

Therefore, the mixture seemsHA/PVP is a desirable and promising field for bone tissue engineering as well as in biomedical applications for bone grafting and repair.

Figure 5 also shows that the polymer chains are connected to each other by a crosslink in the form of a network..

It looks like a flat surface. Therefore, calcium phosphate takes the shape of a mold.PVP is the principle of polymer operation. Based on the above, the molecular arrangement of the components in the polymer matrix can be described as in Figure (6).

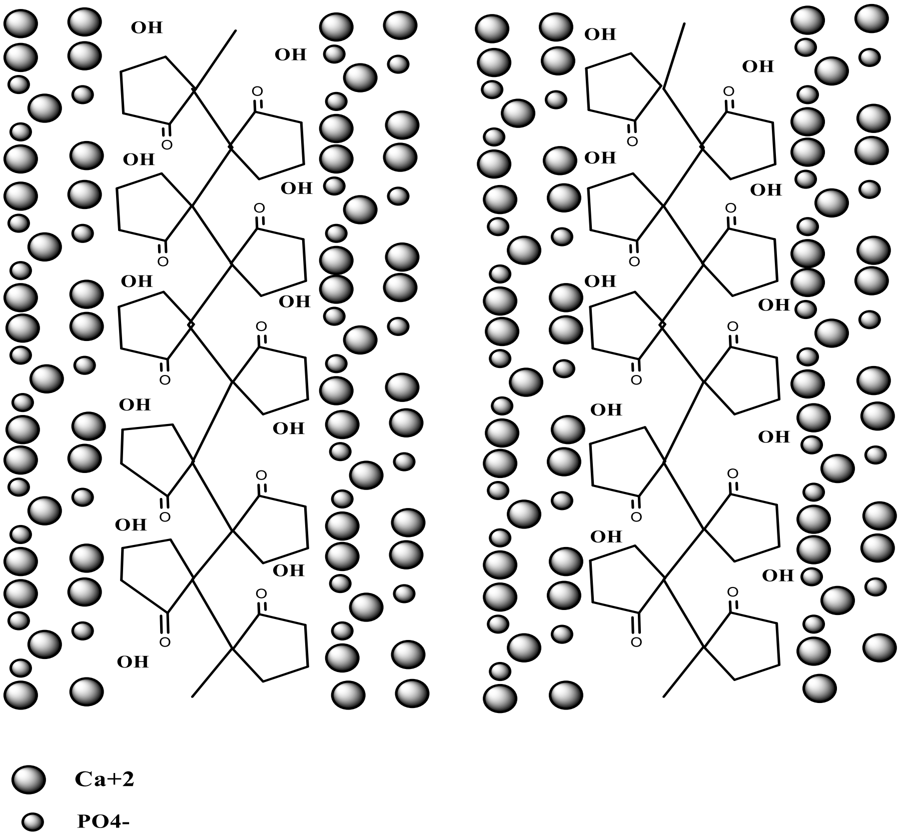

Figure 6. Representing components HA on a PVP polymer matrix.

Understanding the nature of the interaction between the components is extremely important due to its impact on crystal growth and formation. The mechanism and type of bonding between them are still being studied.HA and PVP are not fully understood. It can be assumed that the formation of HA after the addition of PVP can occur through hydrogen and ion bonding.

Studies have confirmed the ability of the carbonyl groupC=O in PVP to form bonds with neighboring molecules, including the hydroxyl group OH in HA.

In our study, the carbonyl group was found from the beginning and before heat treatment, leading to the assumption that its association with the hydroxyl groupOH in HA by hydrogen bonding, where the carbonyl group receives a proton from hydrogen to form the bond, while calcium ions are bonded to the phosphate group as shown in Figure (7).

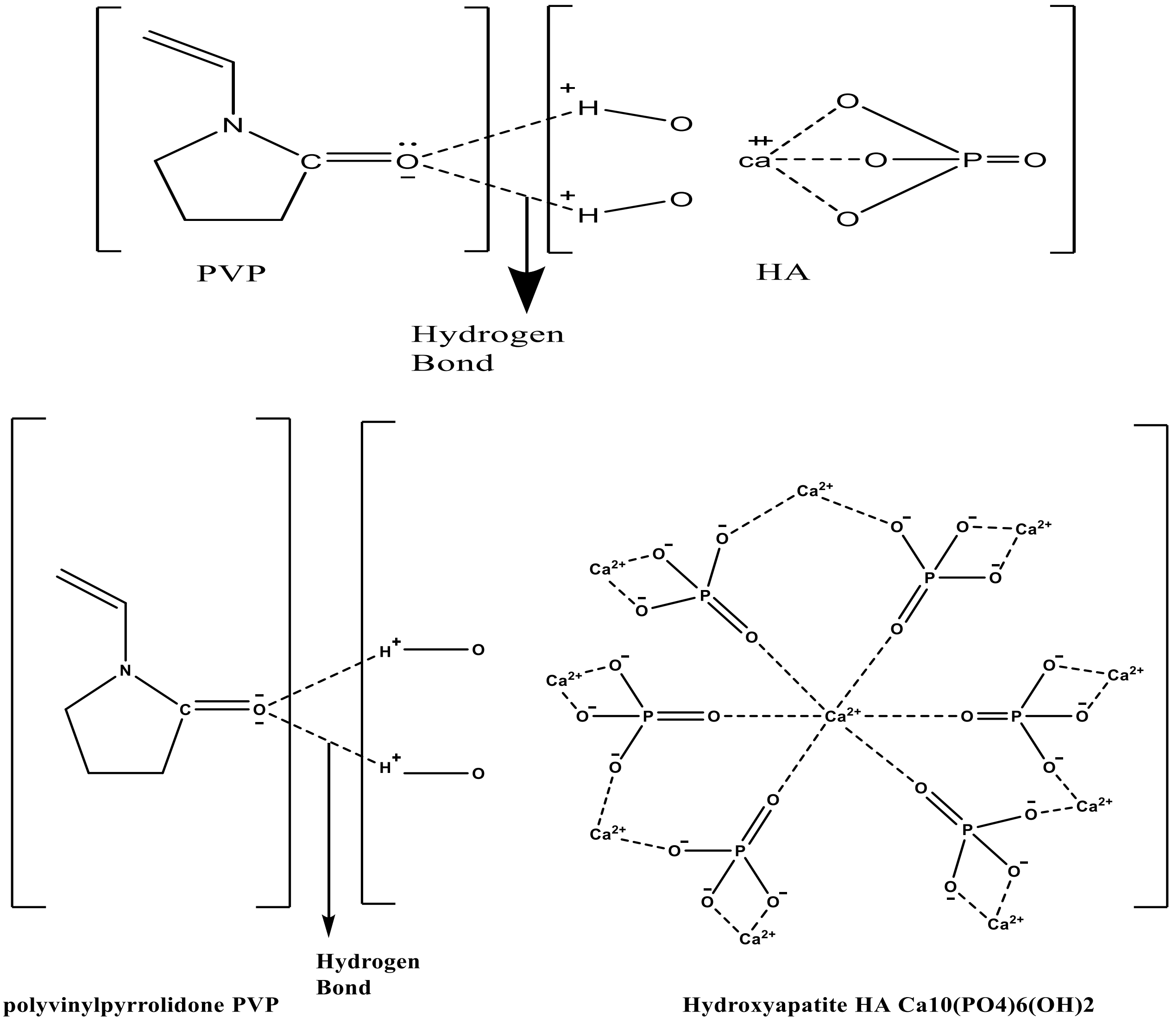

Figure 7. The proposed mechanism for the interactionsPVP with HA through hydrogen bonding.

that interactionPVP interacts with positive metal ions and can be represented by an ionic bond. This means that an ionic bond can be formed between the carbonyl group C=O in PVP and calcium ions, as illustrated in Figure 8. Through this mechanism, the growth of hydroxyapatite and the crystallization of calcium phosphate can be controlled using PVP polymer as a template. Here, the carbonyl group is expected to be adsorbed by the large Ca2+ ions, which in turn attract the PO43- ions to ultimately form HA.

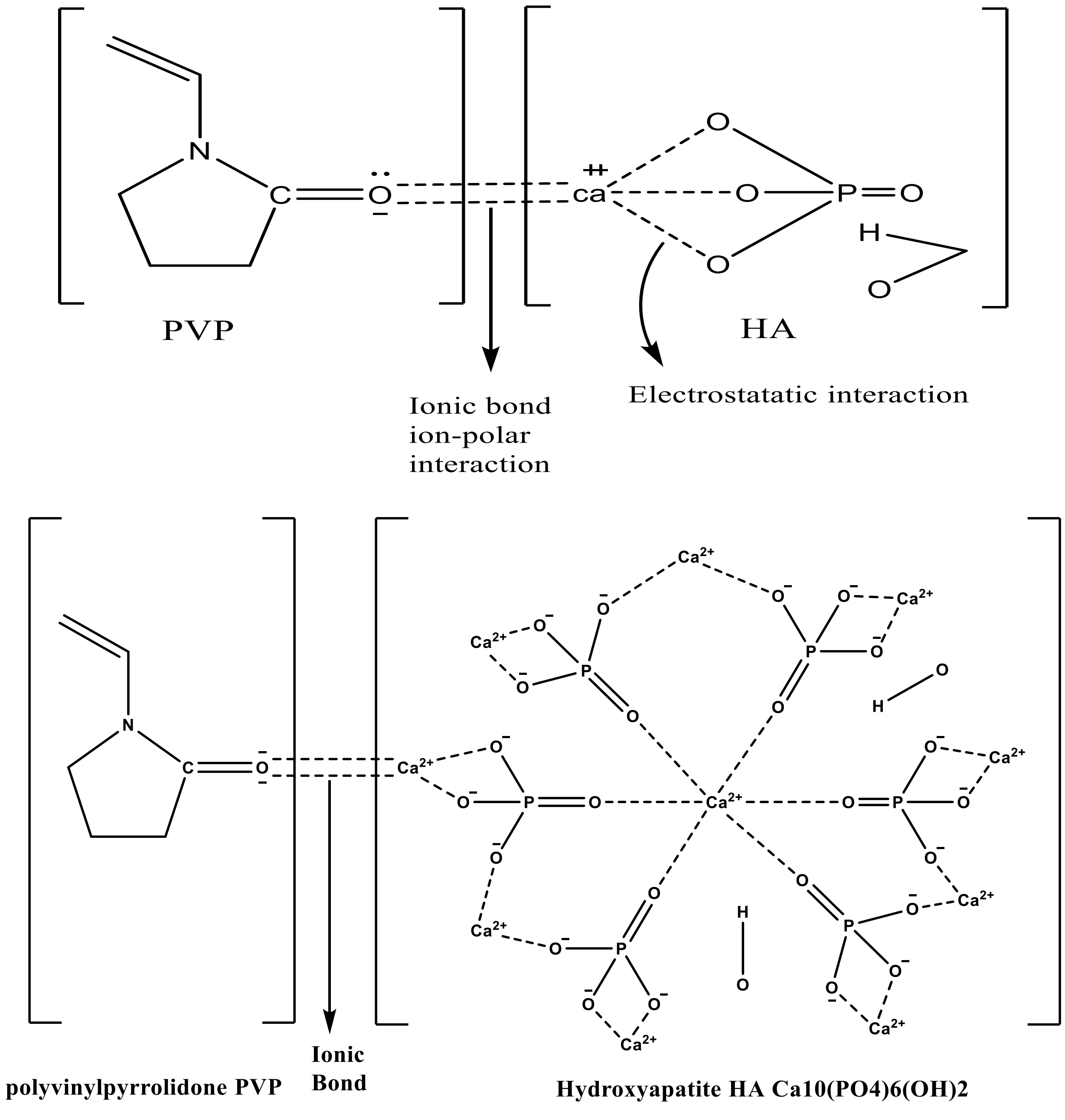

Figure 8. The proposed mechanism for the interactions PVP with HA through ionic bonding.

4. Conclusions:

Based on the results of laboratory studies, it was proven that the resulting mixed films fromPVP and sodium alginate are biocompatible, and in situ CHA synthesis leads to acute cytotoxicity of the composite film, associated with the release of reaction byproducts that create an acidic environment. Ex situ HA-containing materials have been shown to be biocompatible and promising for medical applications in sealing soft tissue defects. Using a light-induced electrochemical resonance spectroscopy (ESR) method, the chemical reaction between HA and PVP was confirmed, and a relationship was established between the ultrafine reaction parameters and the concentration of the PVP polymer. This finding offers a potential opportunity to control the thickness of the polymer layer surrounding the HA molecules, which is important for targeted drug delivery and prolonging therapeutic effects.

5. References :

1. IP Mazur, NA Bakshutova, and DM Stavskaya, “Clinical and microbiological effectiveness of the use of local antimicrobial and antiseptic drugs in the treatment of periodontal diseases,” *Modern Dentistry*, no. 1, pp. 32–39, 2014.
2. AM Sampiev, EB Nikiforova, and AV Sopovskaya, “Current state of research in the field of creating dental films,” *Int. J. Appl. and Fundamental Res.*, no. 3, Part 2, pp. 293–297, 2016.
3. AD Latipova, EV Sysoeva, and MA Sysoeva, “Development of the composition of medicinal films for dentistry,” *Bull. Kazan Technol. Univ.*, vol. 19, p. 22, 2016.
4. VK Leontiev, “A new method of treating inflammatory periodontal diseases,” *Doctor*, no. 3, pp. 22–23, 1997.
5. IY Varpakhovskaya, “New drug delivery systems,” *Remedium*, no. 2, pp. 62–70, 1999.
6. LI Kutsenko, YG Santuryan, EB Karetnikova, IV Gofman, AM Bochek, and EF Panarin, “Study of the bicomponent system methylcellulose-polyvinylpyrrolidone in solution and solid state,” *J. Appl. Chem.*, vol. 80, pp. 792–792, 2007.
7. FP Sidelkovskaya, *Chemistry of N-vinylpyrrolidone and its polymers*, Nauka, 1970, p. 150.
8. J. Rosiak, J. Olejniczak, and A. Charlesby, “Determination of the radiation yield of hydrogels crosslinking,” *Int. J. Radiat. Appl. Instr. Part C. Rad. Phys. Chem.*, vol. 32, pp. 691–694, 1988.
9. IV Fadeeva, EV Rogatkina, AS Fomin, SM Barinov, ES Trofimchuk, and YD Perfil'ev, “Methylcellulose films partially crosslinked by iron compounds,” *Inorg. Mat.: Appl. Res.*, vol. 10, no. 4, pp. 875–878, 2019.
10. IV Fadeeva, ES Trofimchuk, EV Rogatkina, GA Davydova, II Selezneva, OS Antonova, and SM Barinov, “Films based on methylcellulose for medical use,” *Perspective Materials*, no. 5, pp. 38–44, 2017.
11. M. Summa, D. Russo, I. Penna, N. Margaroli, et al., “A biocompatible sodium alginate/povidone iodine film enhances wound healing,” *Eur. J.Pharm. Biopharm.*, vol. 122, pp. 17–24, 2018.
12. H. Li, F. Jiang, S. Ye, Y. Wu, K. Zhu, and D. Wang, “Bioactive apatite incorporated alginate microspheres with sustained drug-delivery for bone regeneration application,” *Mater. Sci. Eng. C*, vol. 62, pp. 779–786, 2016, doi: 10.1016/j.msec.2016.02.012.

13. H.V. Ho, G. Tripathi, J. Gwon, S.Y. Lee, and B.T. Lee, “Novel TOCNF reinforced injectable alginate/β-tricalcium phosphate microspheres for bone regeneration,” *Mater. Des.*, vol. 194, p. 108892, 2020, doi: 10.1016/j.matdes.2020.108892.
14. K. Sangeetha and EK Girija, “Tailor made alginate hydrogel for local infection prophylaxis in orthopedic applications,” *Mater. Sci. Eng. C*, vol. 78, pp. 1046–1053, 2017, doi: 10.1016/j.msec.2017.04.154.
15. TI Vereshchagin, VA Khabas, EA Kulinich, and VP Ignatov, *Ceramic and Glass-Crystalline Materials for Medicine*, Tomsk Publishing House IPU, 2008, p. 151.
16. M. Nabavinia, AB Khoshfetrat, and H. Naderi-Meshkin, “Nano-hydroxyapatite-alginate-gelatin microcapsule as a potential osteogenic building block for modular bone tissue engineering,” *Mater. Sci. Eng. C*, vol. 97, pp. 67–77, 2018, doi: 10.1016/j.msec.2018.12.033.
17. FF Murzakhanov, GV Mamin, MA Goldberg, AV Knotko, MR Gafurov, and SB Orlinsky, “EPR of radiation-induced nitrogen centers in hydroxyapatite: new approaches for studying electron-nuclear interactions,” *Coord. Chem.*, vol. 46, pp. 653–662, 2020, doi: 10.31857/S0132344X20110055.

Al-Hamdaniya Journal for Pure Sciences, Vol:0, No: 0, 2025 (33-42)

The Role of Sunlight and Hydrofluoric Acid Concentration in the Preparation of Porous Gallium Arsenide Wafers

Islam N. Yousif [1*]

[1*] Department of Physics, Education College for Pure Science, University of Al-Hamdaniya, Mosul, Iraq

E-mail: [1*] islam-nasser@uohamdaniya.edu.iq

Abstract

Porous gallium arsenide (n-type) wafers with (111) crystal orientation with low electrical resistivity of (0.00245 Ω.cm) were prepared using photochemical etching technique, relying on sunlight as an alternative light source to artificial sources such as halogen lamps, tungsten lamps, or lasers, due to its high efficiency, low cost, and environmental sustainability. The results of surface morphology analysis using atomic force microscopy (AFM) showed the possibility of obtaining porous layers with diverse surface nature and distinctive nanoscale properties. Experiments were conducted using different concentrations of hydrofluoric acid (HF 40%, HF 30%, HF 25%), with the removal time fixed at (min60) and light intensity of (18167 mW/cm^2), where the results showed that the thickness of the porous layers decreased with decreasing acid concentration, reaching (39.47 nm, 27.40 nm, 15.52 nm) respectively, while the average diameters of the resulting nanoparticles increased, ranging between (55.37 nm, 68.50 nm, 81.70 nm) depending on the acid concentration. It was also found that the surface roughness and thickness of the porous layer increased with increasing HF acid concentration, while these properties decreased with decreasing its concentration. These results demonstrate the importance of the effect of HF acid concentration in controlling the surface morphology of gallium arsenide and the properties of its porous layers, opening the way for the design of customized nanomaterials that meet the needs of advanced applications including nanoelectronics, solar cells, and highly sensitive sensors.

Keywords: Porous Gallium Arsenide, Sunlight, Hydrofluoric Acid, Photoelectrochemical Etching, Porous Layer.

---

1. Introduction

Gallium arsenide (GaAs) was first discovered as one of the important semiconductor materials in the early twentieth century; however, significant interest in it began to grow markedly with the development of electronic and optoelectronic technologies in the mid-twentieth century [1–4]. Over time, researchers recognized the unique capabilities of gallium arsenide, such as its high efficiency in converting light into electricity, chemical stability, and ability to operate in high-frequency applications [5–7]. The first discovery of porous gallium arsenide attracted considerable attention in the early 1990s, when electrochemical etching methods were used to transform the material's surface into a porous structure, leading to enhanced optical properties and an increased effective surface area [8–9].

Porous gallium arsenide technology is considered a major research focus due to its wide range of applications in electronic and optoelectronic devices. The photoelectrochemical etching method using hydrofluoric acid (HF) and sunlight has emerged as one of the innovative approaches for preparing this material. This technique combines chemical reactions with photonic effects to form fine porous structures, where hydrofluoric acid is distinguished by its ability to dissolve surface oxides, while sunlight provides the energy required to stimulate electrochemical reactions on the material's surface [10–12].

In addition, porous gallium arsenide offers exceptional features, including enhanced light absorption and increased surface interaction with the surrounding environment, making it a strong candidate for the development of highly efficient and sensitive sensing technologies [13–14]. Controlling the porous properties of this material enables the fabrication of devices with improved performance tailored to specific applications, such as high-efficiency solar cells and advanced photodetectors [15–17].

This research aims to investigate the effect of various operational parameters, such as hydrofluoric acid concentration and solar irradiation intensity, on the structural and optical properties of porous gallium arsenide. This study represents a vital step toward improving the performance of electronic and optoelectronic devices through the application of efficient and precise fabrication techniques based on a thorough understanding of the porous characteristics of gallium arsenide.

2. Experimental Section

N-type gallium arsenide (GaAs) wafers with a (111) crystallographic orientation and a resistivity of (0.00245 Ω·cm), with dimensions of approximately (1 cm × 0.5 cm), were used and prepared by the photoelectrochemical etching method. This technique belongs to the class of electrode-free methods, meaning that no external voltage or applied current is used during the etching process. Instead, the motion of holes depends on the flow of positive charges from the bottom of the sample toward the top, which occurs as a result of the imbalance in chemical dissolution and the reactions generated on the upper surface of the sample after exposure to sunlight.

Initially, the wafers were immersed in diluted hydrofluoric acid (HF 10%) for nine minutes to remove the native oxide layers. Subsequently, they were rinsed with acetone and ethanol for five minutes to eliminate any remaining HF or adhering impurities, if present. The wafers were then left to dry. After that, the samples were placed in hydrofluoric acid solutions with different concentrations (HF 40%, HF 30%, and HF 25%) inside a Teflon container at a fixed etching time (60 min) and a constant illumination intensity of approximately (18,167 mW/cm²). The HF solution covered the mirror-like surface of the sample, which was fixed facing the light source (sunlight). The sunlight provided a suitable illumination intensity, leading to the formation of a porous layer as a result of generating the required current to support the etching process arising from the motion of positive charge carriers (holes). These charges migrate from the lower dark surface of the wafer (non-etched) toward the upper illuminated surface (etched).

The occurrence of the etching process and the formation of pores on the upper surface of the wafer facing the light source (sunlight) were confirmed by observing the appearance of small bubbles on the GaAs surface, in addition to a noticeable change in its color [18–19]. After completing the etching process, the wafer was placed in a sealed container (tube) filled with methanol to prevent the formation of an oxide layer and to preserve the properties of the sample.

The resulting porous structure of the porous GaAs wafers was carefully examined using an atomic force microscope (AFM), which is considered an essential tool that greatly assists in studying the pore distribution and size on the surface, as well as analyzing the changes occurring in the crystalline structure of these wafers due to the photoelectrochemical reaction. This contributes to a comprehensive and accurate understanding of the properties of the prepared material.

3. Results and Discussion

The results of preparing gallium arsenide wafers demonstrated the formation of a well-defined porous structure uniformly distributed over the upper surface of the wafers after exposure to sunlight and hydrofluoric acid (HF) as a chemical activating agent. Atomic force microscopy (AFM) images revealed a homogeneous distribution of pores across the surface, with variations in pore size and shape depending on the HF concentration and the duration of sunlight exposure. Three porous gallium arsenide samples were prepared using different HF concentrations (HF 40%, HF 30%, and HF 25%), while maintaining a constant etching time of (60 min) and a fixed illumination intensity of (18,167 mW/cm²).

The effect of HF concentration on the surface morphology of the produced porous layer becomes evident when the wafer is immersed in an HF concentration of (40%). The AFM analysis results, shown in Figure (1), indicate the formation of a porous layer with a thickness of (39.47 nm), consisting of quasi-spherical structures with an average diameter of (55.37 nm), as illustrated in Figure (2). The statistical distribution of the formed particles and grains shows diameter ranges between (35→80 nm). The highest volume percentage (20.87%) corresponds to particles and grains with diameters of approximately (55 nm). Meanwhile, the average surface roughness reached (10.3 nm), the root mean square (RMS) roughness value was (11.9 nm), the surface skewness was (0.00171), and the average peak-to-peak distance was (41.3 nm). These results indicate that a suitable surface morphology can be achieved, enabling the wafer to be utilized for the desired applications.

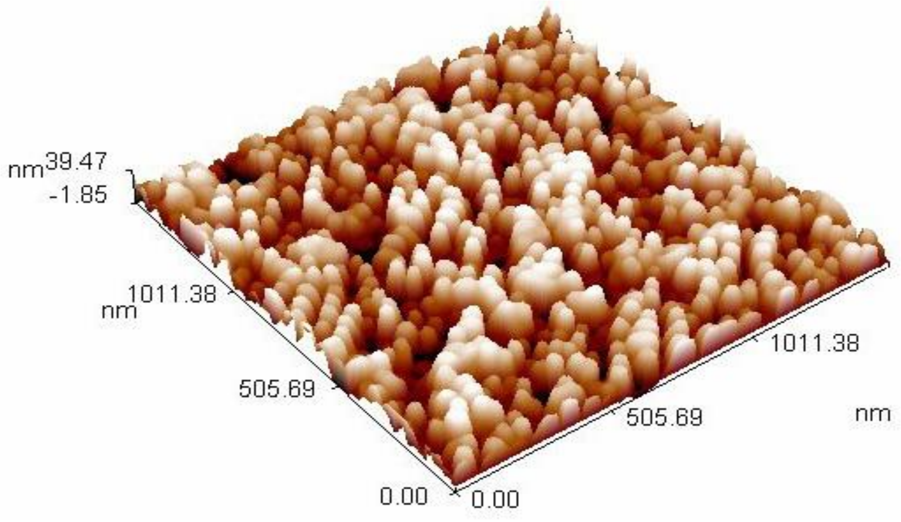

Figure (1): Surface morphology of the gallium arsenide wafer prepared with a hydrofluoric acid concentration of (HF 40%), at a constant illumination intensity of (18,167 mW/cm²) and an etching time of (60 min).

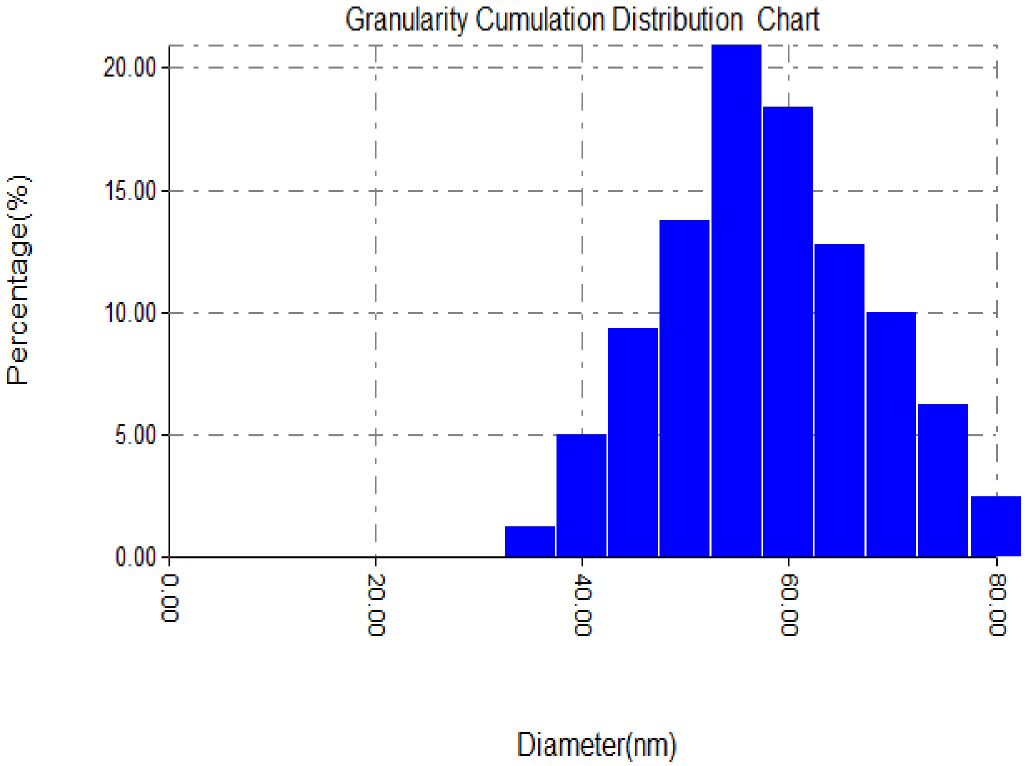

Figure (2): Statistical distribution of the sizes of the nanoparticles and nanograins formed on the surface of the wafer shown in Figure (1).

When a lower HF concentration (30%) is used on another wafer, while all wafer properties and preparation conditions remain similar to those of the previously prepared sample, the atomic force microscopy (AFM) analysis reveals a clear effect of HF concentration on the surface morphology of the resulting porous layer, as shown in Figure (3). This leads to the formation of a porous layer with a thickness of (27.40 nm), composed of quasi-spherical structures with an average diameter of (68.50 nm), as illustrated in Figure (4). The statistical distribution of the formed nanoparticles shows a diameter range between (60→85 nm), with the highest volume percentage (26.75%) corresponding to particles with diameters of approximately (65 nm). Meanwhile, the average surface roughness is (7.05 nm), the root mean square (RMS) roughness value reaches (8.15 nm), the surface skewness is (1.2e-005), and the average peak-to-peak distance is (28.2 nm). These characteristics make this sample a favorable option for applications that require emissions within the visible spectrum.

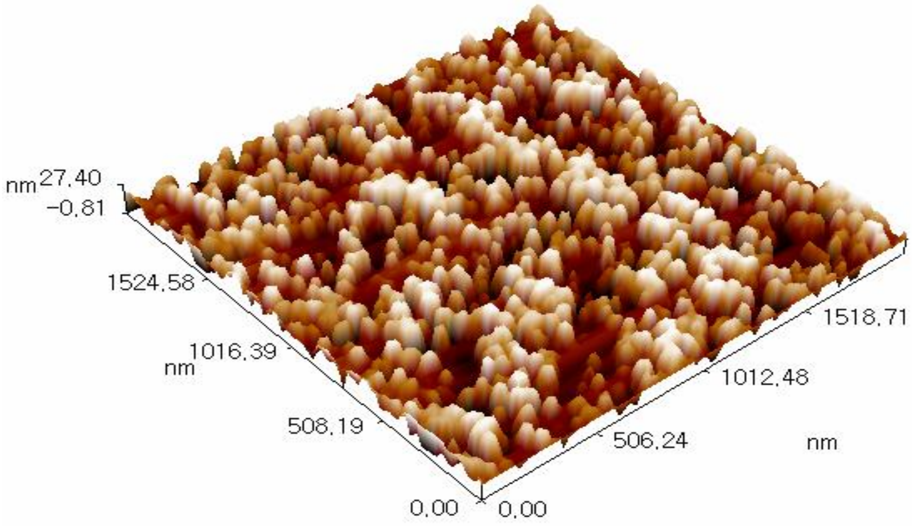

Figure (3): Surface morphology of the gallium arsenide wafer prepared with a hydrofluoric acid concentration of (HF 30%), at a constant illumination intensity of (18,167 mW/cm²) and an etching time of (60 min).

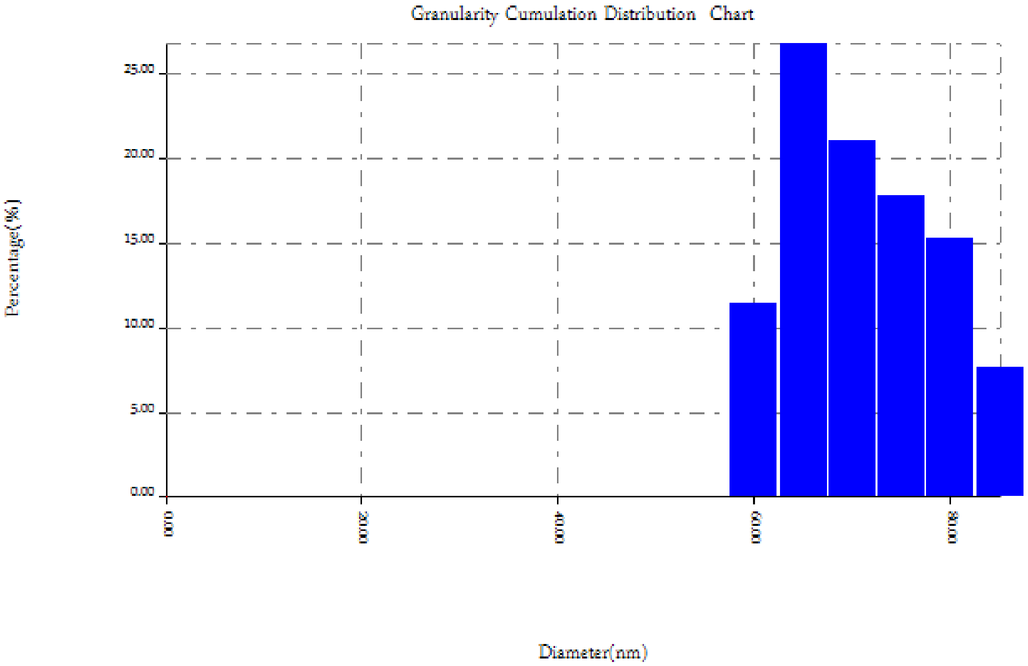

Figure (4): Statistical distribution of the sizes of the nanoparticles and nanograins formed on the surface of the wafer shown in Figure (3).

By further reducing the HF concentration compared to the previous cases to (25%), while keeping the wafer properties and preparation conditions similar to the other prepared samples, the AFM analysis results clearly show a significant effect of HF concentration on the surface morphology of the resulting porous layer, as illustrated in Figure (5). This results in the formation of a porous layer with a thickness of (15.52 nm), composed of quasi-spherical structures with an average diameter of (81.70 nm), as shown in Figure (6). The statistical distribution of the formed nanoparticles shows diameters ranging from (65→140 nm), with the highest volume percentage (19.55%) corresponding to particles with diameters of approximately (75 nm). The average surface roughness is (3.87 nm), the root mean square (RMS) roughness value is (4.48 nm), the surface skewness is (-0.00579), and the average peak-to-peak distance is (15.8 nm). These characteristics provide a foundation for designing tailored nanomaterials to meet the demands of advanced applications.

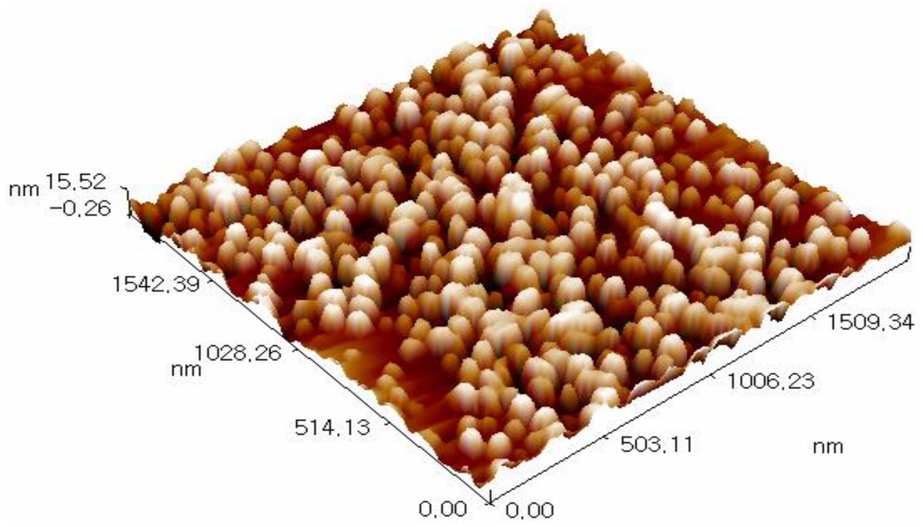

Figure (5): Surface morphology of the gallium arsenide wafer prepared with a hydrofluoric acid concentration of (HF 25%), at a constant illumination intensity of (18,167 mW/cm²) and an etching time of (60 min).

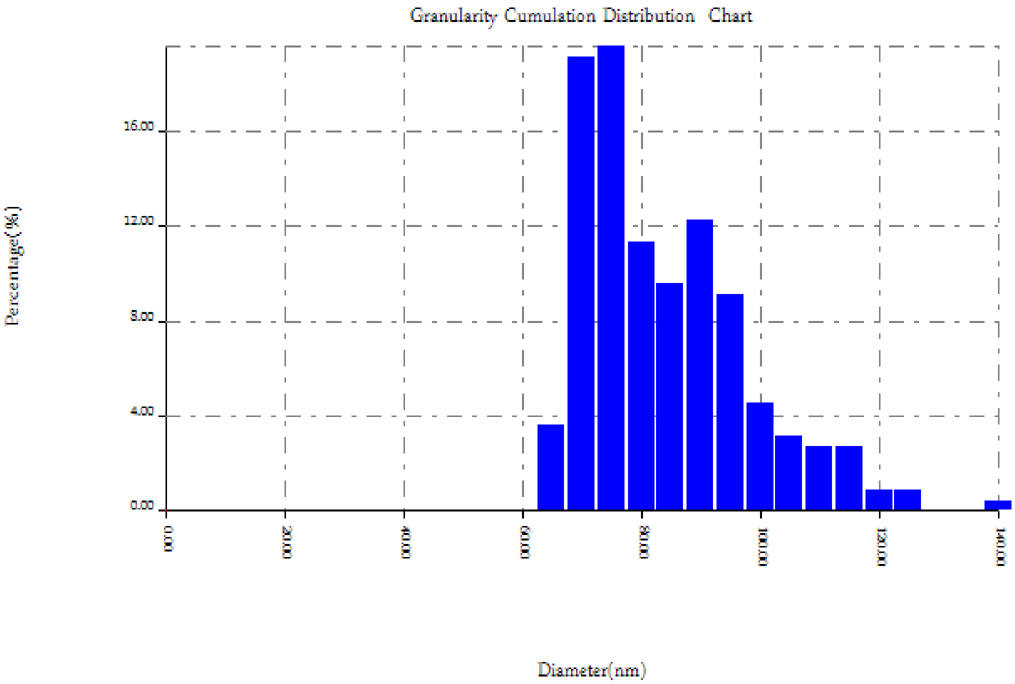

Figure (6): Statistical distribution of the sizes of the nanoparticles and nanograins formed on the surface of the wafer shown in Figure (5).

Furthermore, it is evident from the three produced wafers that surface roughness, porous layer thickness, root mean square (RMS) value, and the average peak-to-peak distance all increase with higher HF concentration and decrease with lower HF concentration, indicating a direct relationship between them. The sizes of the crystalline structures on the surface decrease as the etching progresses; however, nanoparticle or nanograin agglomeration may occur due to the continuation of the etching process, leading to changes in the sizes of the nanostructures. This results in an increase in the diameters of some particles, with the particle diameter range for these wafers varying from (55→65→75 nm). It is also observed that there is a relative variation in the average diameters, which is attributed to the random etching processes occurring on the wafer surface.

4. Conclusion

Porous gallium arsenide wafers prepared using the photoelectrochemical etching technique, with sunlight as the light source and hydrofluoric acid as the chemical agent, represent a promising step in the development of nanomaterials for advanced applications. The results showed that relying on sunlight, as a sustainable and low-cost source, enhances the efficiency of the process while reducing the environmental impacts associated with the use of artificial light sources. Additionally, the choice of hydrofluoric acid as the chemical agent was crucial in achieving high-quality pore formation and a homogeneous surface structure, contributing to the improvement of the optical and electrical properties of the wafers.

This method can provide an innovative solution for producing porous gallium arsenide wafers for various applications, such as solar cells and sensors. However, the environmental and health challenges associated with acid use necessitate the development of safer techniques or the improvement of safety procedures. Future work may focus on optimizing reaction conditions and enhancing the mechanical and structural stability of these wafers to open new horizons for their practical applications.

5. References

[1] G. Spinardi, “Road-mapping, disruptive technology, and semiconductor innovation: the case of gallium arsenide development in the UK,” *Technology Analysis & Strategic Management*, vol. 24, no. 3, pp. 239-251, 2012, doi: 10.1080/09537325.2012.655410.

[2] M. P. Mikhailova, K. D. Moiseev and Y. P. Yakovlev, “Discovery of III–V semiconductors: physical properties and application,” *Semiconductors*, vol. 53, pp. 273-290, 2019.

[3] K. Wakjira, “*Optical properties of GaAs nanostructures* (Doctoral dissertation),” 2019.

[4] H. J. Joyce, C. J. Docherty, Q. Gao, H. H. Tan, C. Jagadish, J. Lloyd-Hughes, L. M. Herz, and M. B. Johnston, “Electronic properties of GaAs, InAs and InP nanowires studied by terahertz spectroscopy,” *Nanotechnology*, vol. 24, no. 21, pp. 214006, 2013, doi: 10.1088/0957-4484/24/21/214006.

[5] H. Helmers, E. Lopez, O. Höhn, D. Lackner, J. Schön, M. Schauerte, M. Schachtner, F. Dimroth, and A. W. Bett, “Pushing the boundaries of photovoltaic light to electricity conversion: A GaAs based photonic power converter with 68.9% efficiency,” In *2021 IEEE 48th Photovoltaic Specialists Conference (PVSC),* (pp. 2286-2289), IEEE, June, 2021, doi: 10.1109/PVSC43889.2021.9518920.

[6] C. Kirchner, M. George, B. Stein, W. J. Parak, H. E. Gaub and M. Seitz, “Corrosion protection and long-term chemical functionalization of gallium arsenide in an aqueous environment,” *Advanced Functional Materials*, vol. 12, no. 4, pp. 266-276, 2002, doi: 10.1002/1616-3028(20020418)12:4<266::AID-ADFM266>3.0.CO;2-U.

[7] N. A. Kulchitsky, A. V. Naumov and V. V. Startsev, “Photonic is a New Driver of Gallium Arsenide Market,” *Photonics Russia*, vol. 14, no. 2, pp. 138-149, 2020, doi: 10.22184/1993-7296.FRos.2020.14.2.138.149.

[8] I. V. Gavrilchenko, Y. S. Milovanov, I. I. Ivanov, A. N. Zaderko, A. P. Oksanich, S. E. Pritchin, M. G. Kogdas, M. I. Fedorchenko, S. N. Goysa and V. A. Skryshevsky, “Luminescent properties of electrochemically etched gallium arsenide,” *Journal of Nano- and Electronic Physics*, vol. 13, no. 4, pp. 04011(6pp), 2021.

[9] H. A. Mohammed, H. A. Kadhem, and I. N. Yousif, “Effect of etching time on gallium arsenide surfaces morphology produced by photochemical etching method using sunlight,” *College Of Basic Education Researches Journal*, vol. 17, no. 2, 2021.

[10] M. C. Traub, “*Chemical functionalization and electronic passivation of gallium arsenide surfaces* (Doctoral dissertation, California Institute of Technology),” 2008, doi: 10.7907/2A4E-HV45.

[11] I. N. Yousif, A. T. Abdulhameed, A. M. Essmat and A. I. Ahmed, “Unraveling the Influence of Hydrofluoric Concentration on the Morphology of Porous Silicon Surfaces Fabricated through Photochemical Etching using Sunlight,” *Iraqi Journal of Applied Physics*, vol. 20, no. 3, 2024.

[12] N. Dmitruk, S. Kutovyi, I. Dmitruk, I. Simkiene, J. Sabataityte and N. Berezovska “Morphology, Raman scattering and photoluminescence of porous GaAs layers,” *Sensors and Actuators B: Chemical*, vol. 126, no. 1, pp. 294-300, 2007, doi: 10.1016/j.snb.2006.12.027.

[13] C. Colombo, M. Heiβ, M. Grätzel and A. Fontcuberta i Morral, “Gallium arsenide pin radial structures for photovoltaic applications,” *Applied Physics Letters*, vol. 94, no. 17, 2009, doi: 10.1063/1.3125435.

[14] M. Wang, J. Yang, S. Liu, Y. Meng, Y. Qin and X. Li, “Metal-Gallium Arsenide Based Tribovoltaic Nanogenerators and its Application for High-Precision Self-Powered Displacement Sensors” *Advanced Materials Technologies*, vol. 8, no. 3, pp. 2200677, 2023, doi: 10.1002/admt.202200677.

[15] H. Saghrouni, A. Missaoui, R. Hannachi and L. Beji, “Investigation of the optical and electrical properties of p-type porous GaAs structure,” *Superlattices and Microstructures*, vol. 64, pp. 507-517, 2013, doi: 10.1016/j.spmi.2013.10.007.

[16] J. Grandidier, D. M. Callahan, J. N. Munday and H. A. Atwater, “Gallium arsenide solar cell absorption enhancement using whispering gallery modes of dielectric nanospheres,” *IEEE Journal of Photovoltaics*, vol. 2, no. 2, pp. 123-128, 2012, doi: 10.1109/JPHOTOV.2011.2180512.

[17] M. Caria, L. Barberini, S. Cadeddu, A. Giannattasio, A. Rusani, A. Sesselego, A. Lai, S. D’Auria and F. Dubecky, “Gallium arsenide photodetectors for imaging in the far ultraviolet region,” *Applied physics letters*, vol. 81, no. 8, pp. 1506-1508, 2002, doi: 10.1063/1.1497996.

[18] I. N. Yousif, M. J. Ali and I. T. Tlayea, “Study the Effect of Etching Time on the Morphology of Porous Silicon Surfaces Manufactured via Photochemical Etching,” *Iraqi Journal of Applied Physics*, vol. 20, no. 3, 2024.

[19] V. Sergey, B. Ihor, V. Viola, S. Yana, K. Olexandr, H. Olga and O. Sergey, “Research into regularities of pore formation on the surface of semiconductors,” *Восточно-Европейский журнал передовых технологий*, vol. 3, no. 5(87), pp. 37-44, 2017.